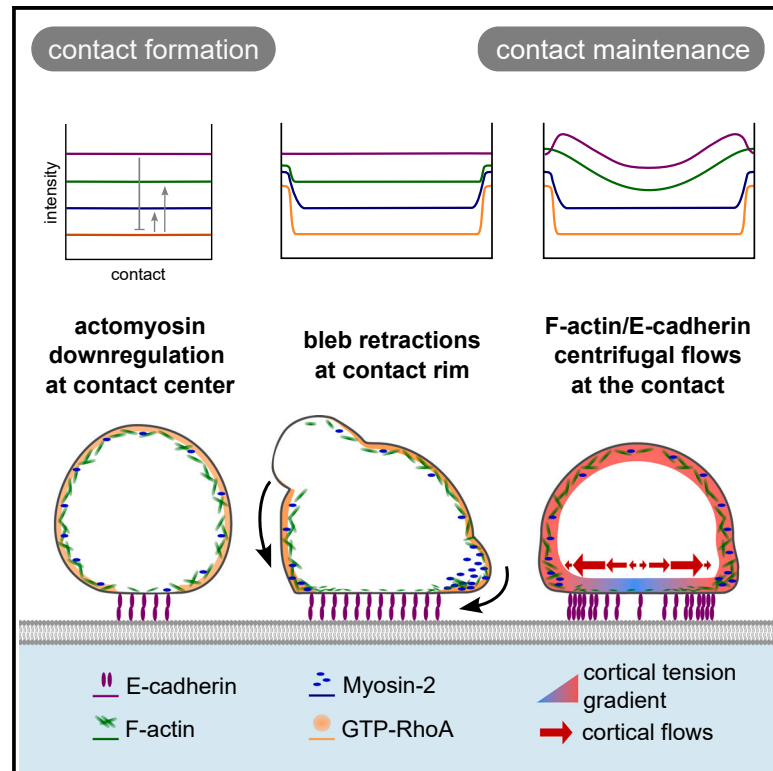Article

Adhesion-induced cortical flows pattern E-cadherin-mediated cell contacts

Graphical abstract

Authors

Feyza Nur Arslan, Édouard Hannezo, Jack Merrin, Martin Loose, Carl-Philipp Heisenberg

Correspondence

heisenberg@ist.ac.at

In brief

Arslan et al. show that the distribution of F-actin and E-cadherin at cell-cell contacts is achieved by a cortical actomyosin tension gradient along the contact radius, established by a combination of E-cadherin signaling and protrusion retraction, driving outward F-actin and E-cadherin flows that lead to their accumulation at the contact rim.

Highlights

- E-cadherin downregulates actomyosin at cell contacts by suppressing RhoA activity

- Blebbing at the cell contact rim increases myosin-2 and cortical tension at the rim

- Graded tension at cell contacts drives centrifugal F-actin flows

- Centrifugal F-actin flows trigger rim accumulation of F-actin and E-cadherin

CellPress

Article

Adhesion-induced cortical flows pattern E-cadherin-mediated cell contacts

Feyza Nur Arslan,[1,2] Édouard Hannezo,[1] Jack Merrin,[1] Martin Loose,[1] and Carl-Philipp Heisenberg[1,3,*]
[1]Institute of Science and Technology Austria, Am Campus 1, Klosterneuburg 3400, Austria
[2]Institute of Bioengineering, École polytechnique fédérale de Lausanne, Lausanne 1015, Switzerland
[3]Lead contact
*Correspondence: heisenberg@ist.ac.at
https://doi.org/10.1016/j.cub.2023.11.067

SUMMARY

Metazoan development relies on the formation and remodeling of cell-cell contacts. Dynamic reorganization of adhesion receptors and the actomyosin cell cortex in space and time plays a central role in cell-cell contact formation and maturation. Nevertheless, how this process is mechanistically achieved when new contacts are formed remains unclear. Here, by building a biomimetic assay composed of progenitor cells adhering to supported lipid bilayers functionalized with E-cadherin ectodomains, we show that cortical F-actin flows, driven by the depletion of myosin-2 at the cell contact center, mediate the dynamic reorganization of adhesion receptors and cell cortex at the contact. E-cadherin-dependent downregulation of the small GTPase RhoA at the forming contact leads to both a depletion of myosin-2 and a decrease of F-actin at the contact center. At the contact rim, in contrast, myosin-2 becomes enriched by the retraction of bleb-like protrusions, resulting in a cortical tension gradient from the contact rim to its center. This tension gradient, in turn, triggers centrifugal F-actin flows, leading to further accumulation of F-actin at the contact rim and the progressive redistribution of E-cadherin from the contact center to the rim. Eventually, this combination of actomyosin downregulation and flows at the contact determines the characteristic molecular organization, with E-cadherin and F-actin accumulating at the contact rim, where they are needed to mechanically link the contractile cortices of the adhering cells.

INTRODUCTION

The spatiotemporal regulation of cell-cell adhesion plays a fundamental role in development and homeostasis.[1,2] Cadherins are central components regulating mechanical adhesion between cells and triggering signaling over the cell-cell contact.[3–6] Malfunction of cadherin-mediated cell-cell adhesion leads to developmental defects and is a marker of cancerous transformations.[7]

Studies on epithelia have provided insight into the mechanisms underlying adherens junction remodeling, showing that E-cadherin (Ecad) junctions at the apical region of cell-cell contacts not only act as biochemical hubs regulating contractility but also as mechanical linkers to the actomyosin network, transmitting forces required for junctional remodeling and integrity.[8–13] Moreover, using culture and embryonic cells to study *de novo* contact formation has highlighted the importance of cadherin-dependent downregulation of the actomyosin cortex at the contact[14–21] and associated accumulation of cadherins at the contact rim, where they are needed to mechanically link the contractile cortices of the adhering cells.[4,17,19,20,22] This rim accumulation of cadherins is mechanosensitive, with tension-induced unfolding of cadherin adhesion components, such as α-catenin and vinculin, increasing mechanical coupling of the adhesion complex to the actomyosin cortex.[1,19,22–24] Yet, how the interplay between cadherins and the actomyosin cortex dynamically structures cell-cell contacts during *de novo* contact

formation remains unclear, mainly due to technical limitations in high-resolution live imaging of entire contacts.

Supported lipid bilayers (SLBs) have been used as assay systems for visualizing and analyzing the dynamic molecular rearrangements at specific cell contacts, such as the immunological synapse.[25] Although lacking the inherent complexity of the cell membrane and underlying cortex, SLBs, as a bottom-up approach, offer the advantage of studying fundamental molecular and cellular processes in a controllable environment. Employing such SLB systems for mimicking Ecad-mediated cell-cell adhesion has shown that Ecad mobility is critical for Ecad recruitment and actin architecture at the contact.[26,27] Still, elucidating how Ecad acquires its distinct distribution at the contact requires supplementing these SLB systems with dynamic and high-resolution imaging of contact formation and maintenance.

Here, we have combined SLBs with high-resolution live imaging to analyze how the dynamic interplay between cadherins and the actomyosin cortex structures cell contacts. Our results suggest that Ecad-signaling-mediated downregulation of cortical actomyosin contractility at the contact center, paired with bleb-retraction-mediated increase in contractility at the contact rim, generates a radial cortical tension gradient. This radial gradient drives centrifugal cortical F-actin flows toward the contact rim, taking along Ecad and thereby leading to the characteristic molecular organization of the contact, with F-actin and Ecad accumulating at the contact rim.
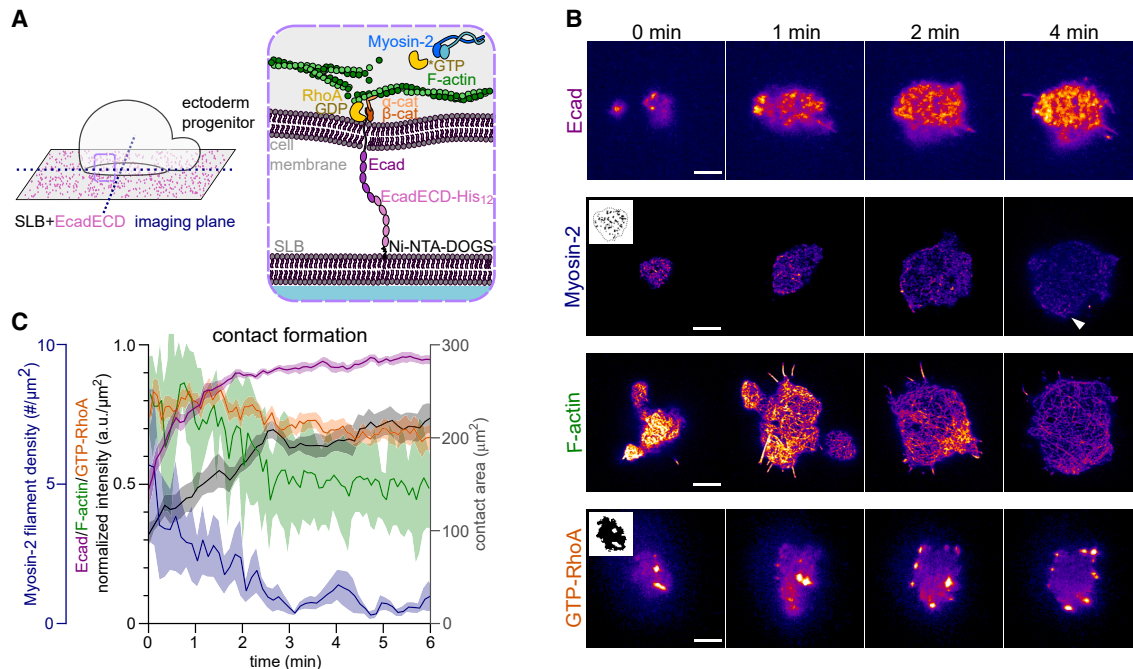
Figure 1. Downregulation of actomyosin and GTP-RhoA coincides with contact area expansion

(A) Schematic of the biomimetic cell adhesion assay. The contact interface between the cell and the EcadECD-functionalized SLB, constituting the imaging plane (left). Close up of the region marked by the dashed rectangle showing the relevant molecular composition of the interface (right).

(B) TIRF (Ecad, GTP-RhoA) or Airyscan (myosin-2, F-actin) cell contact images of Ecad, myosin-2, F-actin, and GTP-RhoA in cells obtained from *Tg(cdh1:mlanYFP)*, *Tg(actb2:Myl12.1-eGFP)*, Ftractin-mNeonGreen-expressing, and GFP-AHPH-expressing embryos at consecutive steps of contact formation. Inlets in myosin-2 and GTP-RhoA images at 0 min are exemplary masks used for mini-filament density (myosin-2) and average intensity (GTP-RhoA) calculations shown in (C). White arrowhead at myosin-2 image at 4 min depicts a bleb. Scale bars, 5 μm.

(C) Plots of contact area (n = 8), myosin-2 mini-filament density (n = 8), Ecad (n = 10), F-actin (n = 6), and GTP-RhoA (n = 11) average intensities at cell contacts during contact formation. Data are mean ± SEM.

See also Figures S1 and S2 and Video S1.

RESULTS

Adhesion signaling regulates cortical actomyosin at the contact by modulating RhoA activity

To visualize cell contact formation dynamics with high spatiotemporal resolution, we established a biomimetic assay where zebrafish ectoderm progenitor cells adhere to SLBs carrying mobile and correctly oriented zebrafish Ecad ectodomains (EcadECD) (Figures 1A and S1A). Given the importance of Ecad mobility for the proper establishment of Ecad-dependent cell-SLB adhesion,[27] we modulated Ecad mobility in the mainly 1,2-dioleoyl-sn-glycero-3-phosphocholine (DOPC)-composed fluid bilayers by adjusting the amounts of Ni^{2+}-loaded 1,2-dioleoyl-sn-glycero-3-[(N-(5-amino-1-carboxypentyl)iminodiacetic acid)succinyl] (Ni-NTA-DOGS) and cholesterol to control Ecad density[28] and bilayer fluidity,[29] respectively (Figure S1B). At molar ratios of 4% Ni-NTA-DOGS and 40% cholesterol, we obtained partially fluid bilayers where tethered EcadECD diffused at $0.34 \pm 0.04\ \mu m^2/s$ and on which seeded ectoderm progenitors were able to form stable contacts (Figure S1C). By contrast, cells adhered less stably when using SLBs lacking EcadECD or progenitor cells with reduced endogenous Ecad expression (*cdh1* morphant cells)[20,30] (Figures S1C and S1D), suggesting that these bilayers constitute a specific biomimetic assay system to analyze Ecad-mediated cell contact formation.

Using this assay system, we first investigated the initial contact formation steps by recording time-lapse movies of newly forming contacts between ectoderm progenitors and EcadECD-decorated SLBs. We used *Tg(cdh1-mlanYFP)* progenitor cells to monitor endogenous Ecad expression[31] and imaged contact formation using total internal reflection fluorescence (TIRF) microscopy to obtain high temporal resolution with minimal photobleaching (Figure S2I). Consistent with previous findings that Ecad accumulates at forming intercellular contacts,[27,32] we found that the concentration of Ecad at the contact increased within the first 2–3 min post contact initiation, which also coincides with the main period of contact expansion (Figures 1B and 1C; Video S1). This increase in Ecad concentrations was not observed in cells seeded on SLBs lacking EcadECD (Figures S2A and S2D) and not accompanied by an accumulation of plasma membrane at the contact (Figures S2B and S2D), suggesting that Ecad trans-binding over the contact leads to Ecad accumulation.[33]

Next, we asked how this Ecad accumulation at the contact relates to potential changes in the organization of the actomyosin cortex at the contact to which Ecad couples.[3] Myosin-2 has previously been shown to be reduced at various mature homotypic contacts.[15,16,18,20] For monitoring changes in myosin-2 at the forming contact, we performed Airyscan microscopy[34] on *Tg(actb2:Myl12.1-eGFP)* progenitor cells,[20,35] obtaining a high spatiotemporal resolution for the myosin-2 signal with minimal

photobleaching (Figure S2I). We found that myosin-2, initially decorating the entire contact as mini-filaments, quickly diminished from the contacts during contact area expansion (Figures 1B and 1C; Video S1). This fast reduction in myosin-2 at the contact led to a nearly complete absence of myosin-2 at the contact 3 min post contact initiation and was temporally closely linked to contact expansion (Figure S2E), as previously suggested.[20] The reduction in myosin-2 depended on the presence of Ecad on both sides of the contact (Figures S2A and S2D) and on Ecad signaling, as the expression of a dominant-negative version of Ecad lacking its cytoplasmic domain (EcadΔcyto) prevented myosin-2 downregulation[36] (Figures S2C and S2D). Notably, the general downregulation of myosin-2 at the contact was accompanied by the sporadic appearance of short-lived myosin-2 accumulations at the contact rim, where cell protrusions such as blebs had retracted (Figure 1B; Video S1).

F-actin, similar to myosin-2, has previously been shown to be partially depleted from the center of mature contacts in several different cell types, including zebrafish ectoderm progenitors.[17,19,20,22] To determine how depletion of myosin-2 at the contact center during contact expansion is accompanied by dynamic alterations of the actin cytoskeleton, we analyzed changes in cortical F-actin network organization at the contact of Ftractin-mNeonGreen-expressing cells using Airyscan microscopy to achieve the highest spatiotemporal resolution with minimal photobleaching (Figure S2I). This analysis showed that the average F-actin intensity decreased at the contact and that this decrease depended on Ecad trans-binding over the contact and signaling (Figures 1B, 1C, S2A, S2C, and S2D; Video S1). Notably, this decrease in F-actin intensity at the contact was less pronounced than the observed depletion of myosin-2 during contact expansion, with some recognizable F-actin cortex remaining still detectable at the mature contact. Collectively, these observations suggest that Ecad contact accumulation is tightly associated with a concomitant reduction in both F-actin and myosin-2, pointing to the possibility that these processes might be functionally linked.

To determine whether such a functional link exists, we analyzed changes in the activity of the small GTPase RhoA, a critical regulator of both F-actin and myosin-2,[37] previously suggested to be modulated upon cadherin binding.[17,18,38,39] To this end, we visualized dynamic changes in RhoA activity during contact formation with an Anillin-based biosensor detecting GTP-RhoA,[40,41] using TIRF microscopy to minimize photobleaching (Figure S2I). Similar to myosin-2 and F-actin, RhoA activity levels decreased at the contact during the first 2–3 min of contact expansion (Figures 1B and 1C; Video S1). By contrast, no such decrease was observed when SLBs were left without EcadECD (Figures S2A and S2D) and when the signaling-defective EcadΔcyto (Figures S2C and S2D) or negative control of the biosensor that does not bind to active RhoA[41] was expressed (Figures S2F and S2F′). This suggests that Ecad trans-binding over the contact and signaling leads to F-actin and myosin-2 downregulation at the forming contact by repressing RhoA activity.

To further challenge this suggestion, we analyzed the colocalization of Ecad and GTP-RhoA at mature contacts (>10 min post contact initiation). This analysis revealed very little overlap and a negative correlation between Ecad clusters and RhoA activity

(Figures S2G–S2G″), consistent with the notion that Ecad binding leads to local repression of RhoA activity. To further test whether Ecad controls F-actin and myosin-2 at the contact by downregulating RhoA activity, we asked whether this effect can be suppressed by constitutively activating RhoA in the contacting cell. To this end, we analyzed contact formation using progenitor cells expressing a constitutively active version of RhoA (CA-RhoA).[42,43] We found that CA-RhoA-expressing progenitors, in contrast to wild-type (WT) controls, showed high RhoA activity at the contact and, consequently, failed to downregulate F-actin and myosin-2 during contact expansion (Figures S2H and S2H′). This suggests that the downregulation of RhoA activity represents a critical effector mechanism by which Ecad reduces actomyosin at the contact.

Myosin-2 asymmetry leads to centrifugal flows of F-actin and Ecad at the contact

Previous studies have shown that both F-actin and different components of the cadherin adhesion complex, such as α-catenin, β-catenin, and Ecad, accumulate at the cell contact rim and that this is required for mechanically coupling the contractile actomyosin cortices of the adhering cells over the contact.[17,19,20,22] To determine whether such distinct spatial localization can also be observed in our biomimetic assay, we first analyzed the average radial distributions of myosin-2, F-actin, Ecad, and GTP-RhoA at mature contacts when their total intensities had reached steady state (Figure S2I). Myosin-2 and GTP-RhoA were nearly completely depleted from the contact, except for some accumulations at places on the contact rim where cellular protrusions, mainly resembling cellular blebs, had retracted (Figure 2A). Averaging this distribution gave rise to myosin-2 and GTP-RhoA sharply peaking at the contact rim (Figure 2A). By contrast, F-actin and Ecad displayed more graded distributions along the contact radius, with increasing levels from the middle toward the rim of the contact (Figure 2A).

To dissect the mechanisms by which the actomyosin cortex and adhesion apparatus remodel at contacts, we first determined to what extent this remodeling depends on Ecad binding over the contact. Analyzing contacts of cells placed on SLBs lacking EcadECD showed that Ecad, myosin-2, F-actin, and GTP-RhoA at the contact remained homogeneously distributed (Figure S3A), suggesting that contact remodeling occurs downstream of Ecad trans-binding and signaling. Next, we asked how the specific distributions of Ecad, myosin-2, F-actin, and GTP-RhoA at mature contacts are established by monitoring changes in their rim-to-center distributions during Ecad-mediated contact formation. Although F-actin, myosin-2, and Ecad became increasingly localized to the contact rim during the entire contact expansion phase (~0–3 min post contact initiation), GTP-RhoA levels were already sharply downregulated at the contact center 1 min after contact initiation, with only some active RhoA remaining at the contact rim (Figure S3B). This shows that the redistribution and rim accumulation of F-actin, myosin-2, and Ecad is preceded by a fast downregulation of RhoA activity at the contact center upon contact initiation.

One possibility by which downregulation of RhoA activity at the contact center might trigger the continuous relocalization of F-actin and Ecad to the contact rim is by building up an actomyosin contractility gradient along the contact radius, peaking at
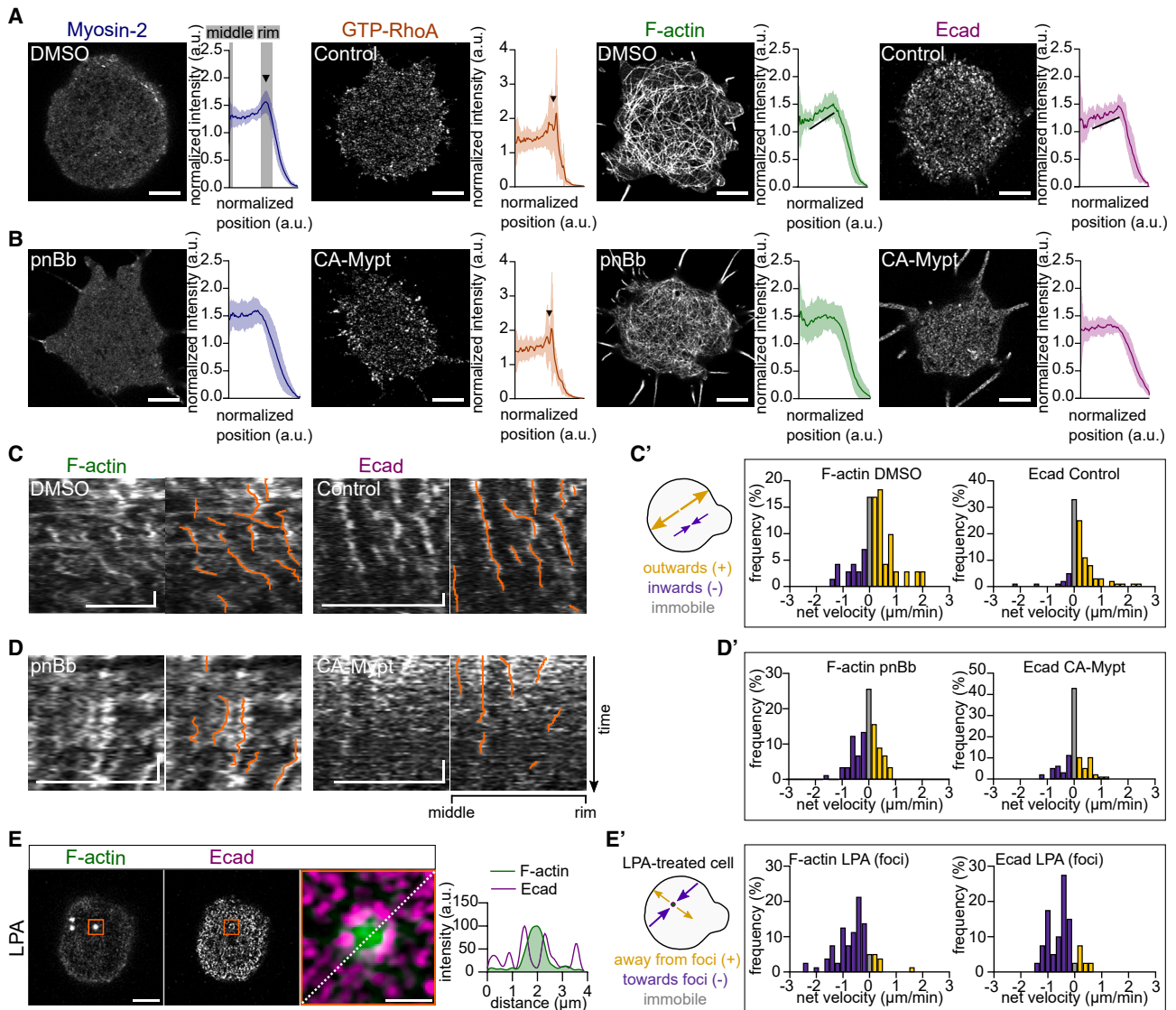
Figure 2. F-actin and Ecad flow toward the contact rim and accumulate there

(A and B) Airyscan images of myosin-2, GTP-RhoA, F-actin, and Ecad in cells obtained from *Tg(actb2:Myl12.1-eGFP)*, GFP-AHPH-expressing, Ftractin-mNeonGreen-expressing, and *Tg(cdh1:mlanYFP)* embryos, along with radial intensity plots of myosin-2 (DMSO: n = 26, pnBb: n = 20) and F-actin (DMSO: n = 20, pnBb: n = 24) at mature contacts (>10 min after contact initiation) of DMSO or pnBb-treated cells, and GTP-RhoA (control: n = 20, CA-Mypt: n = 3) and Ecad (control: n = 20, CA-Mypt: n = 25) at mature contacts of uninjected control and CA-Mypt-injected cells. Black arrowheads in myosin-2 and GTP-RhoA plots depict intensity peaks at the contact rim, black lines in F-actin and Ecad plots depict gradual intensity increases. Data are mean ± SEM.

(C and D) Kymographs along mature contact radius of cells treated with DMSO (as control) or pnBb obtained from Ftractin-mNeonGreen-expressing embryos labeling F-actin, and control or CA-Mypt-expressing cells obtained from *Tg(cdh1:mlanYFP)* labeling Ecad. Detected flow tracks (orange) are superimposed on the raw data.

(C′ and D′) Histograms of F-actin (n = 7, 70 tracks; mean ± SD = 0.22 ± 0.09 μm/min) and Ecad (n = 10, 100 tracks; mean ± SD = 0.25 ± 0.17 μm/min) flow velocities at mature contacts in control conditions, and pnBb-treated (F-actin: n = 11, 110 tracks; mean ± SD = −0.07 ± 0.15 μm/min) or CA-Mypt-expressing (Ecad: n = 10, 100 tracks; mean ± SD = −0.01 ± 0.13 μm/min) cells, color-coded with yellow for centrifugal/outward-directed, purple for centripetal/inward-directed, and gray for immobile tracks (see schematic on the left).

(E) F-actin and Ecad at the mature contact of a cell treated with LPA obtained from Ftractin-mKO2-expressing *Tg(cdh1:mlanYFP)* embryos. Zoomed-in image at a region of the cell contact (marked by the orange rectangle), where ectopic F-actin foci had formed upon LPA treatment. Line plot shows F-actin and Ecad intensity profiles along the dashed line.

(E′) Histograms of F-actin (n = 5, 7 foci, 50 tracks; mean ± SD = −0.66 ± 0.79 μm/min) and Ecad (n = 4, 4 foci, 40 tracks; mean ± SD = −0.5 ± 0.47 μm/min) flow velocities, color-coded with yellow for tracks directed away and purple for tracks directed toward the foci, and gray for immobile tracks (see schematic on the left), at regions of LPA-treated mature contacts showing ectopic F-actin foci, in cells obtained from Ftractin-mNeongreen-expressing wild-type (WT) or Ftractin-mKO-expressing *Tg(cdh1:mlanYFP)* embryos.

Scale bars: 5 and 1 μm in (E, right). Vertical scale bars, 1 min.

See also Figures S3 and S4, Table S1, and Videos S2 and S3.

the contact rim. This contractility gradient might again give rise to centrifugal F-actin network flows, which, by slowing down at the contact rim, could lead to rim accumulation of F-actin and Ecad. Consistent with this possibility, we noticed that although total F-actin intensity at the contact remained unchanged after the initial phase of contact expansion (Figure 1C), F-actin intensity at the contact center continued decreasing for another ~2 min (up to ~5 min post contact initiation) (Figures S3B, S3C, and S3C′). This continuous decrease in intensity was accompanied by a decrease in F-actin network density at the contact center and the emergence of an F-actin network density gradient along the contact radius (Figures S3C, S3C′, and S3D), an effect compatible with the possibility of centrifugal F-actin network flows changing F-actin network density along the flow direction.[44,45] To more directly determine whether the F-actin network indeed displays centrifugal flows at the contact, we performed a kymograph analysis of actin filament movements at the contact. Strikingly, this revealed a net centrifugal flow of F-actin network at the contact (Figures 2C and 2C′; Video S2), slowing down at the contact rim (Figure S3E). The outward direction of flows became apparent only after the initial phase of contact expansion and were also detectable in mature contacts (Figures S3F–S3F″). Together, this suggests that F-actin network dilution at the contact center and progressive accumulation at the contact rim are achieved and maintained by centrifugal F-actin flows after contact expansion.

To understand how the downregulation of RhoA activity at the contact center might lead to the buildup of an actomyosin contractility gradient and flow along the contact radius, we turned to myosin-2, a main determinant of cortical F-actin contractility.[46–49] Specifically, we hypothesized that downregulation of RhoA at the contact center might lead to the near complete depletion of myosin-2 in the center, thereby generating a sharp gradient of myosin-2 activity along the contact radius (Figure 2A). To address this hypothesis, we reduced myosin-2 activity in the contacting cells by exposing cells to the myosin-2 inhibitor para-nitroblebbistatin (pnBb)[50] or by expressing a constitutively active form of myosin phosphatase (CA-Mypt)[43,51] (Figure 2B; note that for analyzing the effect of myosin-2 inhibition on GTP-RhoA and Ecad distributions, we had to use CA-Mypt instead of pnBb, as the autofluorescence of pnBb strongly decreased their signal-to-noise ratios). Cells exposed to pnBb showed strongly diminished centrifugal F-actin flows (Figures 2D, 2D′, and S4A; Video S2) and, as a result of this, reduced F-actin network dilution and contact rim accumulation (Figures 2B and S4B). By contrast, pnBb treatment/CA-Mypt expression did not affect the initial signaling-dependent reduction in average F-actin intensity levels during contact formation and concomitant restriction of GTP-RhoA activity to the contact rim (Figures 2B and S4C). This suggests that centrifugal flows of F-actin are predominantly needed for F-actin network density gradient formation and maintenance.

To further explore whether and how the centrifugal flows of F-actin are related to the graded distribution and accumulation of Ecad at the contact rim, we analyzed dynamic changes in Ecad distribution at the contact. Given that Ecad clusters have previously been shown to be taken along by F-actin flows,[52–54] we hypothesized that the observed centrifugal F-actin flows at the contact center might trigger similar flows of Ecad, leading to Ecad

gradient formation and contact rim accumulation. Kymograph analysis revealed Ecad clusters to flow centrifugally, with an average net velocity similar to F-actin filaments (Figures 2C, 2C′, and S4A; Video S3), pointing to the possibility that centrifugal F-actin flows take along Ecad toward the contact rim. Consistent with this, distinct Ecad clusters showed partial colocalization with F-actin filaments at the contact (Figures S3G–S3G″), suggesting that some, but not all, Ecad clusters might be directly linked to F-actin. To further challenge the functional link between F-actin and Ecad flows, we tested whether myosin-2 inhibition affects not only F-actin but also Ecad localization and flows. Blocking myosin-2 activity with pnBb—while leaving the average intensity of Ecad at the contact unchanged (Figure S4C)—eliminated Ecad rim accumulation, leading to a homogeneous distribution of Ecad across the contact (Figure S4D), similar to the observations made for F-actin in the presence of pnBb (Figures 2B and S4C). To determine whether the lack of Ecad rim accumulation upon inhibition of myosin-2 activity is due to reduced centrifugal flows of Ecad, we performed a kymograph analysis of Ecad flows in cells with reduced myosin-2 activity. CA-Mypt-expressing cell contacts not only showed more homogeneous Ecad and F-actin intensities and higher F-actin network densities (Figures 2B, S4B, and S4E), similar to the observations made when blocking myosin-2 activity with pnBb (Figures 2B and S4D), but also displayed strongly reduced centrifugal flows of Ecad clusters (Figures 2D, 2D′, and S4A; Video S3). This suggests that Ecad clusters might be advected by the F-actin network flows toward the contact rim in a myosin-2-dependent manner.

To further challenge this suggestion, we asked whether upregulating myosin-2-dependent actin network contractility is sufficient for driving F-actin and Ecad centrifugal flows. To this end, we treated cells with lysophosphatidic acid (LPA), which has been shown to strongly enhance actomyosin contractility in progenitor cells.[22,45] Upon exposure to LPA, F-actin, and to a smaller extent also Ecad, showed an enhanced accumulation at the contact rim, giving rise to steeper gradients of F-actin and Ecad along the radial axis of the contact (Figure S4F). Notably, the average intensities of F-actin and Ecad at the contact did not change upon LPA treatment (Figure S4C), suggesting that LPA treatment affects the distribution but not the average amount of these proteins at the contact. Unexpectedly, however, radial flow velocities of F-actin and Ecad, and the network density of F-actin at the contact center, remained unchanged in LPA-treated contacts (Figures S4A, S4B, S4E′, and S4F′; Videos S2 and S3). Rather, we frequently observed ectopic foci of actomyosin within the contact center (Figures 2E and S4G), presumably as a result of high actomyosin contractility leading to the emergence of local network instabilities and thus the formation of ectopic actomyosin foci, driving local flows of F-actin and Ecad directed toward them[45,55] (Figures 2E′ and S4A). Collectively, these findings suggest that the polarized distribution of myosin-2 triggers flows of both F-actin and Ecad, thereby establishing their graded distribution along the contact radius.

Cortical flows at the contact determine the contact architecture

To determine whether and how the observed changes in F-actin and Ecad rim accumulations in the different experimental conditions can be explained by centrifugal F-actin flows at the contact,
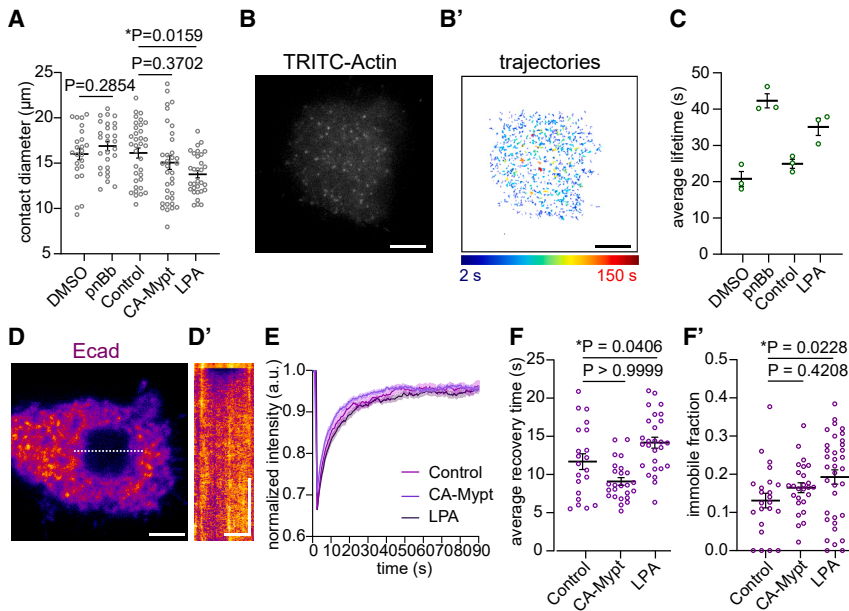
Figure 3. Actomyosin contractility affects contact size and F-actin/Ecad molecular turnover

(A) Mature contact (>10 min after contact initiation) diameters of control (DMSO-treated [0.1%] [n = 24] or untreated [n = 35]), pnBb-treated (n = 28), CA-Mypt-expressing (n = 36), and LPA-treated (n = 31) cells.

(B) TIRF image of TRITC-actin at single-molecule resolution at a mature contact.

(B′) Time trajectories of TRITC-actin molecules, tracked over 6 min. Color map indicates the trajectory durations.

(C) TRITC-actin average lifetimes at mature contacts for control conditions (DMSO or untreated), and cells treated with pnBb or LPA. Each open circle represents 3 different time lapses obtained on the same day.

(D) TIRF image of Ecad at the mature contact of a cell obtained from *Tg(cdh1:mlanYFP)* embryos, at the first post-bleach frame during FRAP measurements.

(D′) Kymograph of Ecad recovery obtained from intensity profiles along the dashed line shown in (D).

(E) Exemplary recovery curves of Ecad intensity within bleached regions normalized to pre-bleach intensity at the mature contacts of cells obtained from *Tg(cdh1:mlanYFP)* embryos for untreated control (n = 11), CA-Mypt-overexpression (n = 9), and LPA treatment (n = 9).

(F) Ecad recovery times after photobleaching at mature contacts of untreated control (n = 35), CA-Mypt-expressing (n = 24), and LPA-treated (n = 28) cells obtained from *Tg(cdh1:mlanYFP)* embryos.

(F′) Immobile fractions of Ecad at mature contacts, obtained for the data described in (F).

Scale bars, 5 μm. Vertical scale bars, 1 min.

Data are mean ± SEM. Student's t test, DMSO control, and pnBb (A); Kruskal-Wallis test control, CA-Mypt, and LPA (A, F, and F′).

See also Figure S5 and Table S1.

we sought to quantitatively link F-actin flows to F-actin and Ecad rim accumulation, which seemed to dominate contact remodeling after the contact expansion phase. From a theoretical perspective, the strength of this accumulation not only depends on centrifugal flow velocity v but also contact size L and protein turnover/lifetime τ at the contact. A simple conservation equation taking into account these features predicts that at first order, the magnitude of the rim-to-center accumulation A should scale as $A = 1 + v \frac{2\pi^2 \tau}{L}$. To test this quantitatively, we measured contact size and actin/Ecad lifetimes under different conditions. For contact size, we found that LPA-treated contacts were smaller than untreated controls, consistent with previous observations from progenitor cell-cell doublets[22] (Figure 3A). By contrast, the size of pnBb-treated/CA-Mypt-expressing contacts, although expected to decrease,[22] remained largely unchanged, likely due to a global decrease in cortical tension leading to cell flattening on the substrate. To measure actin turnover, we tracked tetramethylrhodamine (TRITC)-actin protein injected at low amounts using single-molecule imaging at the contact (Figures 3B and 3B′). We found a lifetime of ~25 s for actin monomers, which was increased on average by both increasing or decreasing contractility by LPA and pnBb, respectively, in line with previous reports[19,56] (Figure 3C). For Ecad lifetime at the contact, we turned to fluorescence recovery after photobleaching (FRAP) experiments (Figures 3D, 3D′, and 3E). Similar to previous observations on α-catenin turnover at Ecad-mediated ectoderm cell-cell contacts,[22] we found an Ecad recovery time of ~12 s and a small immobile fraction of ~10%, which were both increased when upregulating actomyosin contractility upon LPA treatment

(Figures 3F and 3F′). By contrast, decreasing contractility through the expression of CA-Mypt had no recognizable effect on Ecad dynamics (Figures 3F and 3F′).

Having measured contact size, Ecad/F-actin turnover, and flow velocities (Table S1), we then tested whether the predicted analytical relationship between Ecad/F-actin centrifugal flows and rim accumulation would hold across different contractility conditions and found that the two displayed a robust positive scaling, as expected in the analytical expression (Figure 4A). Explicitly integrating the conservation equation in space (1D along the rim-center axis) and time, starting from a homogeneous distribution, showed that contacts reached a steady-state distribution profile in a few minutes (Figure S5A), closely matching the F-actin and Ecad distributions for most experimental conditions (Figures 4B and S5B). Notably, predicted F-actin distributions underestimated the accumulation seen at LPA-treated contacts, suggesting that there might be other factors, in addition to flow velocity, contact size, and protein turnover, that also influence F-actin rim accumulations in the presence of LPA. Collectively, this comparison between simulations and experimental observations shows that the progressive accumulation of F-actin and Ecad at the contact rim can largely be explained by the centrifugal flows of these proteins at the contact.

Blebs establish the radial cortical tension gradient at the contact

To understand how the flows of F-actin and Ecad were generated and directed, we followed up on our initial observation of
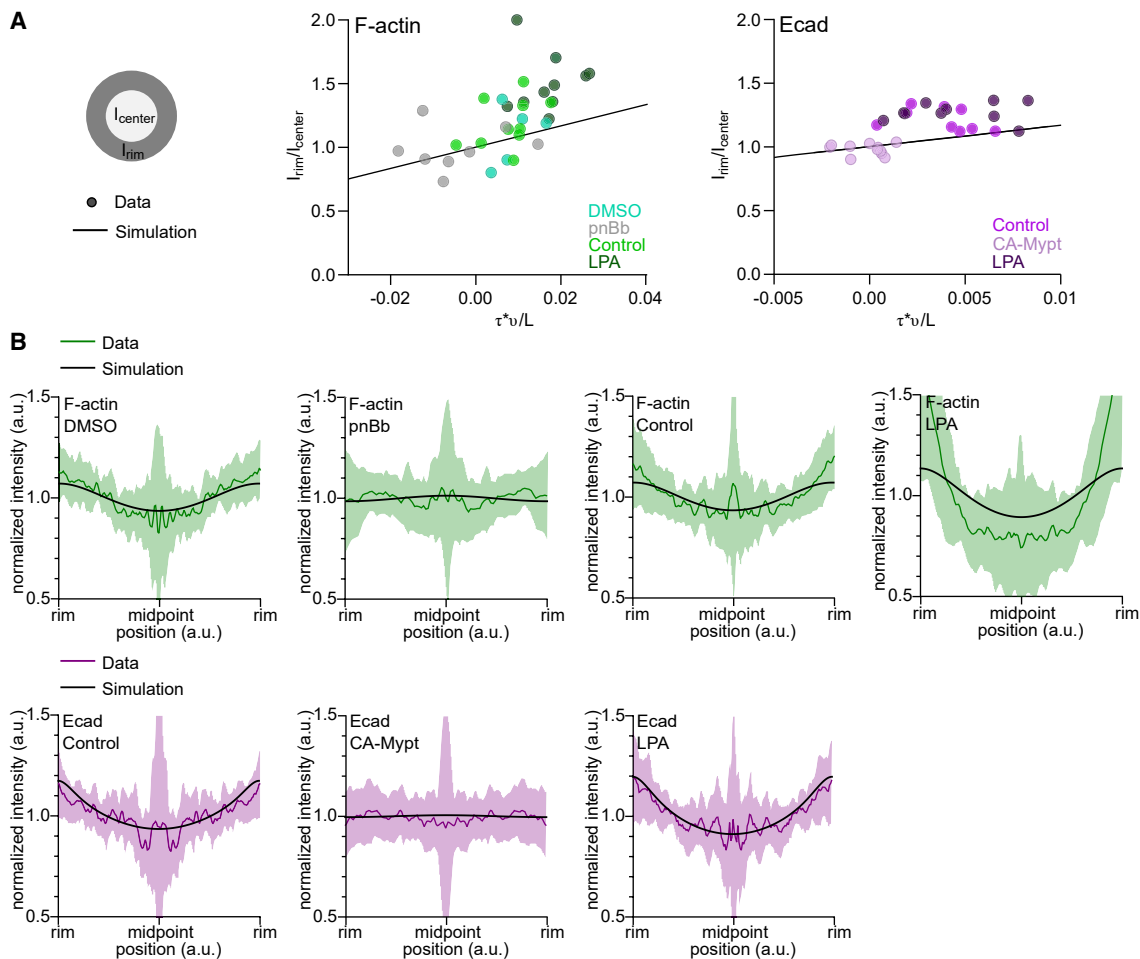
Figure 4. Contractility-dependent flow velocity and molecular turnover determine spatial distribution of F-actin and E-cadherin at the mature contact

(A) Plots of rim-to-center intensity ratios for F-actin or Ecad as a function of parameters predicting rim enrichment—molecular lifetime (τ) * flow velocity (v)/contact diameter (L)—across different contractility conditions. Dots represent individual mature contacts for which rim-to-center intensity ratios (see schematic on the left), flow velocities, and contact diameters were measured. Molecular lifetimes were taken from Table S1. Lines indicate the predicted values of rim enrichment based on the equation $A = 1 + v\frac{2\pi^2}{L}\tau$ (see STAR Methods). F-actin in DMSO control (n = 6), pnBb-treated (n = 8), untreated control (n = 12), or LPA-treated (n = 10) cells, and Ecad in untreated control (n = 11), CA-Mypt-expressing (n = 11), or LPA-treated (n = 10) cells obtained from Ftractin-mNeonGreen-expressing and *Tg(cdh1:mlanYFP)* embryos.

(B) Theoretically predicted steady-state F-actin and Ecad intensity profiles based on the equation given in (A) using experimentally measured parameters (Table S1; STAR Methods). In the same plots, radial F-actin and Ecad intensity plots, normalized to rim-to-rim distance, taken from the experiments shown in Figures 2A, 2B, S4E′, and S4F′ are shown.

See also Figure S5 and Table S1.

myosin-2 accumulations at places of the contact rim, where cellular protrusions, mainly blebs, had retracted (Figure 2A). In line with previous reports showing the assembly of a myosin-2-rich F-actin cortex during bleb retraction,[57] we found that the formation of typically observed cellular blebs at the contact rim (Figure S4H) was temporally linked to an increase in myosin-2 and that myosin-2 accumulation at the rim was locally linked to bleb retraction (Figures S4I and S4J; Video S1). To further explore whether these local accumulations lead to direct F-actin flows, we performed a kymograph analysis comparing rim regions where blebs retracted to regions where no such blebs formed. Strikingly, this analysis revealed faster and more directed flows of F-actin toward retracting

blebs (Figure S4K), supporting the notion that local bleb-driven myosin-2 accumulations at the contact rim drive and direct these flows.

To more directly assess whether cell blebbing is the mechanism maintaining rim contractility and centrifugal flows by accumulating myosin-2 at the contact rim, we overexpressed a constitutively active form of Ezrin2 (CA-Ezrin2), a membrane-cortex linker previously used for reducing blebbing in progenitor cells.[58] We found that reduced blebbing and contact areas upon CA-Ezrin2 expression were accompanied by decreased GTP-RhoA, myosin-2, F-actin, and Ecad accumulations at the contact rim (Figures 5A, S4L, and S4M). Although the overall levels of F-actin and Ecad at the contact were unaffected by CA-Ezrin2
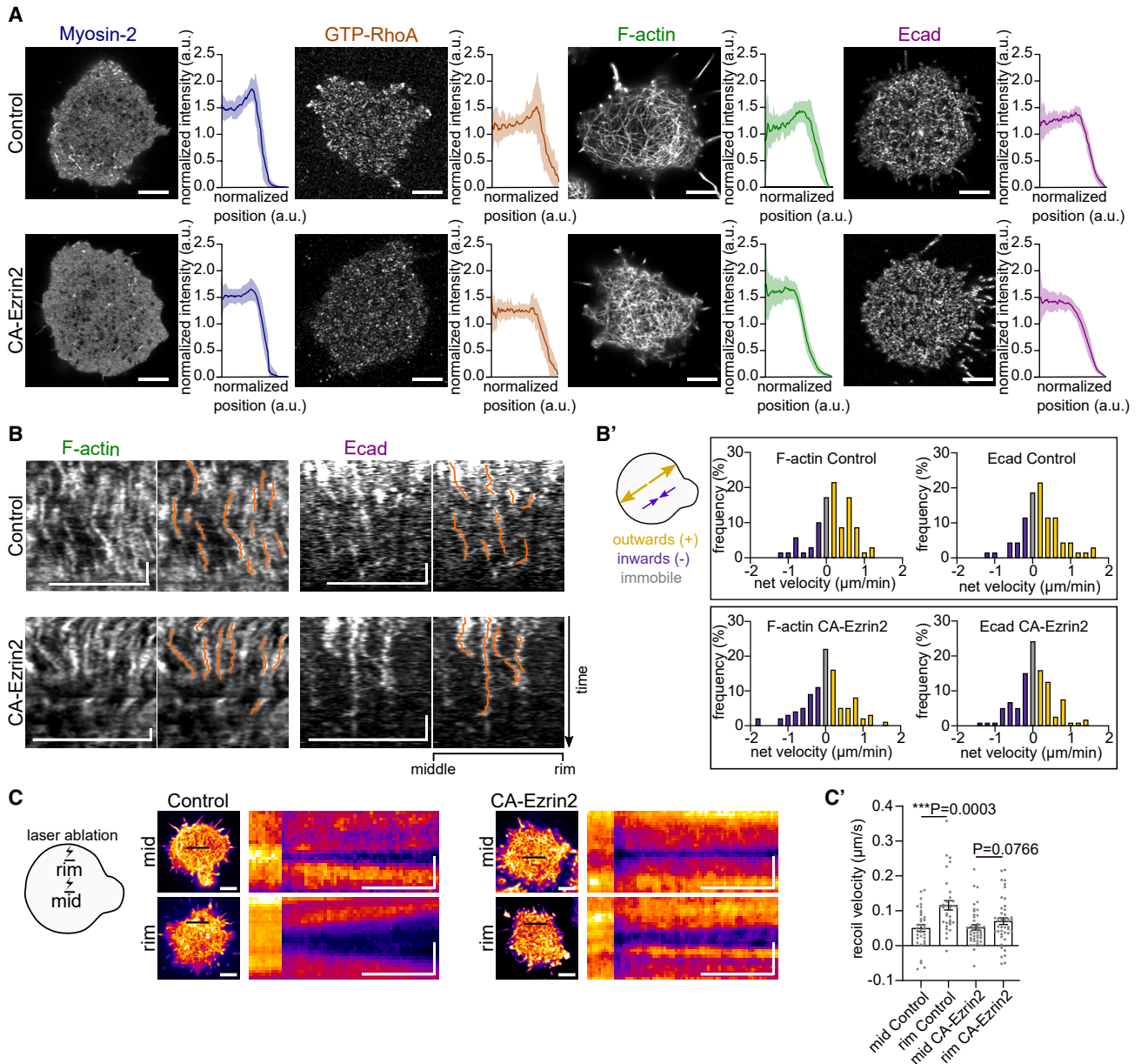
Figure 5. Bleb retractions at the contact rim direct cortical flows by establishing a cortical tension difference

(A) Airyscan images of myosin-2, GTP-RhoA, F-actin, and Ecad at mature contacts (>10 min post contact initiation) of cells obtained from control or CA-Ezrin2-expressing *Tg(actb2:Myl12.1-eGFP)*, GFP-AHPH-expressing, Ftractin-mNeonGreen-expressing, and *Tg(cdh1:mlanYFP)* embryos, along with radial intensity plots of myosin-2 (control: n = 18, CA-Ezrin2: n = 43), GTP-RhoA (control: n = 32, CA-Ezrin2: n = 29), F-actin (control: n = 17, CA-Ezrin2: n = 36), and Ecad (control: n = 26, CA-Ezrin2: n = 40).

(B) Kymographs of F-actin and Ecad flows along the mature contact radius in cells obtained from Ftractin-mNeonGreen-expressing and *Tg(cdh1:mlanYFP)* embryos, expressing or not expressing (control) CA-Ezrin2. Detected flow tracks (orange) are superimposed on the raw data.

(B′) Flow velocity histograms of F-actin and Ecad at mature contacts for control (F-actin: n = 7, 70 tracks; mean ± SD = 0.16 ± 0.5 μm/min; Ecad: n = 7, 70 tracks; mean ± SD = 0.21 ± 0.52 μm/min), and CA-Ezrin2-expressing (F-actin: n = 10, 100 tracks; mean ± SD = −0.03 ± 0.65 μm/min; Ecad: n = 13, 130 tracks; mean ± SD = 0.03 ± 0.48 μm/min) cells; color-coded with yellow for centrifugal/outward-directed, purple for centripetal/inward-directed, and gray for immobile tracks (see schematic on the left).

(C) Pre-cut frames and kymographs of F-actin recoil at mature contacts of control or CA-Ezrin2-expressing cells obtained from Ftractin-mNeonGreen-expressing embryos, upon UV laser ablations along indicated lines at the middle or rim of the contacts (see schematic on the left).

(C′) Plot of initial recoil velocities after UV laser ablation for the conditions shown in (C). Control middle (n = 34), control rim (n = 33), CA-Ezrin2-expressing middle (n = 44), and CA-Ezrin2-expressing rim (n = 45). Mann-Whitney U test.

Scale bars: 5 μm, 1 μm in kymograph (C). Vertical scale bars: 1 min in (B) and 1 s in (C).

Data are mean ± SEM.

See also Figure S4, Table S1, and Videos S2, S3, and S4.

overexpression (Figure S4C), their net flows toward the rim vanished (Figure 5B) and, consistently, F-actin network density at the contact center remained high (Figure S4B). This indicates that cell blebbing is a critical mechanism for maintaining rim contractility and centrifugal Ecad/F-actin flows.

To directly test whether the F-actin and Ecad flows were directed via a bleb-mediated cortical tension gradient between the contact middle and rim, we measured cortical tension oriented along the contact radius using UV laser ablations.[35] We found that in WT contacts, cortical tension was significantly higher at the contact rim as opposed to the middle, consistent with the presence of a radial cortical tension gradient (Figures 5C and 5C'; Video S4). This tension gradient depended on normal blebbing activity in the contacting cells, as the expression of CA-Ezrin2 abolished the tension gradient by lowering the contact rim tension to the level found at the contact middle (Figures 5C and 5C'; Video S4). In contrast, when cells were plated on SLBs lacking EcadECD, CA-Ezrin2 expression had no effect on cortical tension at the cell-SLB interface (Figures S4N and S4N'), suggesting that cell blebbing is specifically needed for building up the radial tension gradient at functional cell contacts. Together, these data indicate that blebbing is required for myosin-2 to accumulate at the contact rim, resulting in a radial cortical tension gradient, which again directs centrifugal flows of F-actin and Ecad, establishing their rim accumulation.

DISCUSSION

Our study identifies the mechanistic basis by which cell contacts acquire their specific molecular organization during contact formation and maintenance. We show that centrifugal F-actin flows, triggered by the depletion of myosin-2 at the contact center and concomitant accumulation at the contact rim, take along Ecad by advection, leading to F-actin and Ecad accumulation at the contact rim, where they are needed for coupling the cortices of the contacting cells. Notably, such centrifugal flows likely reflect an emergent property of the actomyosin network at the contact, a possibility we tested using an active gel model[59] (Figure S5C). Assuming a fixed contact size during flow establishment (Figures 1C and S2F–S2F") and higher actomyosin contractility at the contact rim (Figure 5C) as a starting configuration, the model predicted long-range F-actin network centrifugal flows, similar to those observed experimentally (Figure S5B; see STAR Methods), which were reinforced and maintained by the resulting accumulation of F-actin at the contact rim. This suggests that the molecular organization of the contact is an expression of the emergent properties of the actomyosin network.

On a molecular level, our data suggest that downregulation of the actomyosin cortex at the contact center is mediated by signaling from trans-bound Ecad downregulating GTP-RhoA (Figures S2A, S2C, and S2D).[38,39] Several Ecad downstream effectors previously implicated in RhoA activity modulation, such as Rac kinase,[17] p120-catenin,[38] and various RhoGAPs,[60,61] might be involved in this downregulation, while their specific roles in mediating RhoA downregulation still need to be established. Our data suggest that their effect is overridden by bleb-retraction-mediated transient accumulation of myosin-2 at the contact rim. This spatially confined blebbing activity at the contact rim is likely due to trans-bound cadherins strengthening membrane-to-

cortex adhesion[62] at the contact center and/or Ecad accumulating at the contact slightly away from the periphery where RhoA/actin/myosin-2 accumulate (Figure S3H). Such spatial segregation has previously been described[17,19,63,64] and is also apparent at the ectopic foci observed in LPA-treated contacts (Figures 2E and S4G). Although the underlying mechanisms driving such segregation are yet unclear, reduced binding affinity of Ecad to the rim F-actin network due to changes in network architecture and/or membrane height differences between the contact rim and center, might be involved.[64–68]

Bleb-mediated rim accumulations of actomyosin could also explain the observed increased accumulation of actomyosin in LPA-treated cells, considering that these cells show increased blebbing at the contact rim due to their higher contractility[45,69] (Figures S4F and S4L). Why this increased actomyosin rim accumulation did not lead to faster centrifugal flows (Figures S4A and S4F') is still unclear. LPA-induced increases in F-actin cortex viscosity and/or friction (Figure S5C; see STAR Methods), and interference with the global centrifugal F-actin flow pattern by the ectopic actomyosin foci forming at the contact centers (Figures 2E, 2E', and S4G), might be responsible for this.

Our biomimetic cell contact assay using SLBs is reductionist in nature, which can be an advantage when studying changes in the behavior of specific molecules but also a disadvantage due to the lack of a natural cell membrane and cortex on the SLB side of the contact. Although our molecular turnover measurements at cell-bilayer contacts do not markedly differ from reported values from cell-cell contacts[22] (Figure 3F), suggesting that the SLB does not strongly interfere with the molecular dynamics at the contact, increasing the complexity of biomimetic assays by adding transmembrane proteins and cytoskeleton could lead to an even more faithful representation of cell-cell contact formation and remodeling in vivo.

Ecad has previously been shown to be transported by F-actin flows, a process implicated in junctional remodeling between epithelial cells and contact initiation between migrating cells.[52,70–72] F-actin flows, again, are thought to be triggered by the asymmetric distribution of F-actin and/or myosin-2. Our data suggest that the characteristic molecular architecture emerging at the forming contact between cells depends on F-actin-driven Ecad flows. Centrifugal movements of Ecad clusters during contact maturation have previously been noted,[19,32] but their association with the F-actin cortex remained unclear. Our study, by mechanistically linking the dynamic changes in the F-actin cortex to the redistribution of the Ecad adhesion complex at the contact, provides a generic mechanism by which the maturing contact achieves its specific molecular organization required for contact expansion and maintenance. More generally, it might also explain how cells acquire stable polarity during contact formation by locally remodeling their actomyosin cortex, thereby mechanistically linking cell-cell contact formation to cell polarization in the developing organism.

STAR★METHODS

Detailed methods are provided in the online version of this paper and include the following:

- KEY RESOURCES TABLE
- RESOURCE AVAILABILITY

SUPPLEMENTAL INFORMATION

Supplemental information can be found online at https://doi.org/10.1016/j.cub.2023.11.067.

AUTHOR CONTRIBUTIONS

F.N.A. and C.-P.H. designed the research. F.N.A. performed the experiments and analyzed the experimental data. E.H. performed numerical simulations and modeling. J.M. designed and produced the wafers for polydimethylsiloxane (PDMS) confiners. M.L. provided reagents, conceptual input, and support with analysis. F.N.A. and C.-P.H. wrote the manuscript. All authors edited the manuscript.

REFERENCES

1. Pannekoek, W.-J., de Rooij, J., and Gloerich, M. (2019). Force transduction by cadherin adhesions in morphogenesis. F1000Res. *8*. F1000 Faculty Rev-1044.

2. Gumbiner, B.M. (2005). Regulation of cadherin-mediated adhesion in morphogenesis. Nat. Rev. Mol. Cell Biol. *6*, 622–634.

3. Maître, J.-L., and Heisenberg, C.-P. (2013). Three functions of cadherins in cell adhesion. Curr. Biol. *23*, R626–R633.

4. Winklbauer, R. (2015). Cell adhesion strength from cortical tension - an integration of concepts. J. Cell Sci. *128*, 3687–3693.

5. Niessen, C.M., Leckband, D., and Yap, A.S. (2011). Tissue organization by cadherin adhesion molecules: dynamic molecular and cellular mechanisms of morphogenetic regulation. Physiol. Rev. *91*, 691–731.

6. Arslan, F.N., Eckert, J., Schmidt, T., and Heisenberg, C.-P. (2021). Holding it together: when cadherin meets cadherin. Biophys. J. *120*, 4182–4192.

7. Berx, G., and van Roy, F. (2009). Involvement of members of the cadherin superfamily in cancer. Cold Spring Harb. Perspect. Biol. *1*, a003129.

8. Pinheiro, D., and Bellaïche, Y. (2018). Mechanical force-driven adherens junction remodeling and epithelial dynamics. Dev. Cell *47*, 3–19.

9. Munjal, A., and Lecuit, T. (2014). Actomyosin networks and tissue morphogenesis. Development *141*, 1789–1793.

10. Ratheesh, A., Gomez, G.A., Priya, R., Verma, S., Kovacs, E.M., Jiang, K., Brown, N.H., Akhmanova, A., Stehbens, S.J., and Yap, A.S. (2012). Centralspindlin and α-catenin regulate Rho signalling at the epithelial zonula adherens. Nat. Cell Biol. *14*, 818–828.

11. Lecuit, T., and Yap, A.S. (2015). E-cadherin junctions as active mechanical integrators in tissue dynamics. Nat. Cell Biol. *17*, 533–539.

12. Martin, A.C., Gelbart, M., Fernandez-Gonzalez, R., Kaschube, M., and Wieschaus, E.F. (2010). Integration of contractile forces during tissue invagination. J. Cell Biol. *188*, 735–749.

13. Acharya, B.R., Nestor-Bergmann, A., Liang, X., Gupta, S., Duszyc, K., Gauquelin, E., Gomez, G.A., Budnar, S., Marcq, P., Jensen, O.E., et al. (2018). A mechanosensitive RhoA pathway that protects epithelia against acute tensile stress. Dev. Cell *47*, 439–452.e6.

14. Stevens, A.J., Harris, A.R., Gerdts, J., Kim, K.H., Trentesaux, C., Ramirez, J.T., McKeithan, W.L., Fattahi, F., Klein, O.D., Fletcher, D.A., et al. (2023). Programming multicellular assembly with synthetic cell adhesion molecules. Nature *614*, 144–152.

15. Maître, J.L., Niwayama, R., Turlier, H., Nédélec, F., and Hiiragi, T. (2015). Pulsatile cell-autonomous contractility drives compaction in the mouse embryo. Nat. Cell Biol. *17*, 849–855.

16. Chan, E.H., Chavadimane Shivakumar, P., Clément, R., Laugier, E., and Lenne, P.-F. (2017). Patterned cortical tension mediated by N-cadherin controls cell geometric order in the Drosophila eye. eLife *6*, e22796.

17. Yamada, S., and Nelson, W.J. (2007). Localized zones of Rho and Rac activities drive initiation and expansion of epithelial cell-cell adhesion. J. Cell Biol. *178*, 517–527.

18. Hashimoto, H., and Munro, E. (2019). Differential expression of a classic cadherin directs tissue-level contractile asymmetry during neural tube closure. Dev. Cell *51*, 158–172.e4.

19. Engl, W., Arasi, B., Yap, L.L., Thiery, J.P., and Viasnoff, V. (2014). Actin dynamics modulate mechanosensitive immobilization of E-cadherin at adherens junctions. Nat. Cell Biol. *16*, 587–594.

20. Maître, J.-L., Berthoumieux, H., Krens, S.F.G., Salbreux, G., Jülicher, F., Paluch, E., and Heisenberg, C.-P. (2012). Adhesion functions in cell sorting by mechanically coupling the cortices of adhering cells. Science *338*, 253–256.

21. Chu, Y.S., Thomas, W.A., Eder, O., Pincet, F., Perez, E., Thiery, J.P., and Dufour, S. (2004). Force measurements in E-cadherin–mediated cell doublets reveal rapid adhesion strengthened by actin cytoskeleton remodeling through Rac and Cdc42. J. Cell Biol. *167*, 1183–1194.

22. Slováková, J., Sikora, M., Arslan, F.N., Caballero-Mancebo, S., Krens, S.F.G., Kaufmann, W.A., Merrin, J., and Heisenberg, C.-P. (2022). Tension-dependent stabilization of E-cadherin limits cell-cell contact expansion in zebrafish germ-layer progenitor cells. Proc. Natl. Acad. Sci. USA *119*, e2122030119.

23. Huveneers, S., Oldenburg, J., Spanjaard, E., van der Krogt, G., Grigoriev, I., Akhmanova, A., Rehmann, H., and de Rooij, J. (2012). Vinculin associates with endothelial VE-cadherin junctions to control force-dependent remodeling. J. Cell Biol. *196*, 641–652.

24. Buckley, C.D., Tan, J., Anderson, K.L., Hanein, D., Volkmann, N., Weis, W.I., Nelson, W.J., and Dunn, A.R. (2014). The minimal cadherin-catenin complex binds to actin filaments under force. Science *346*, 1254211.

25. Dustin, M.L. (2009). Supported bilayers at the vanguard of immune cell activation studies. J. Struct. Biol. *168*, 152–160.

26. Andreasson-Ochsner, M., Romano, G., Håkanson, M., Smith, M.L., Leckband, D.E., Textor, M., and Reimhult, E. (2011). Single cell 3-D platform to study ligand mobility in cell–cell contact. Lab Chip *11*, 2876–2883.

27. Biswas, K.H., Hartman, K.L., Yu, C.H., Harrison, O.J., Song, H., Smith, A.W., Huang, W.Y.C., Lin, W.-C., Guo, Z., Padmanabhan, A., et al. (2015). E-cadherin junction formation involves an active kinetic nucleation process. Proc. Natl. Acad. Sci. USA *112*, 10932–10937.

28. Thompson, C.J., Vu, V.H., Leckband, D.E., and Schwartz, D.K. (2019). Cadherin extracellular domain clustering in the absence of trans-interactions. J. Phys. Chem. Lett. *10*, 4528–4534.

29. Glazier, R., and Salaita, K. (2017). Supported lipid bilayer platforms to probe cell mechanobiology. Biochim. Biophys. Acta Biomembr. *1859*, 1465–1482.

30. Babb, S.G., and Marrs, J.A. (2004). E-cadherin regulates cell movements and tissue formation in early zebrafish embryos. Dev. Dyn. *230*, 263–277.

31. Cronan, M.R., and Tobin, D.M. (2019). Endogenous tagging at the cdh1 locus for live visualization of E-cadherin dynamics. Zebrafish *16*, 324–325.

32. Adams, C.L., Chen, Y.-T., Smith, S.J., and Nelson, W.J. (1998). Mechanisms of epithelial cell–cell adhesion and cell compaction revealed by high-resolution tracking of E-cadherin– green fluorescent protein. J. Cell Biol. *142*, 1105–1119.

33. Wu, Y., Jin, X., Harrison, O., Shapiro, L., Honig, B.H., and Ben-Shaul, A. (2010). Cooperativity between trans and cis interactions in cadherin-mediated junction formation. Proc. Natl. Acad. Sci. USA *107*, 17592–17597.

34. Huff, J. (2015). The Airyscan detector from ZEISS: confocal imaging with improved signal-to-noise ratio and super-resolution. Nat. Methods *12*. i-ii.

35. Behrndt, M., Salbreux, G., Campinho, P., Hauschild, R., Oswald, F., Roensch, J., Grill, S.W., and Heisenberg, C.-P. (2012). Forces driving epithelial spreading in zebrafish gastrulation. Science *338*, 257–260.

36. Levine, E., Lee, C.H., Kintner, C., and Gumbiner, B.M. (1994). Selective disruption of E-cadherin function in early Xenopus embryos by a dominant negative mutant. Development *120*, 901–909.

37. Sit, S.-T., and Manser, E. (2011). Rho GTPases and their role in organizing the actin cytoskeleton. J. Cell Sci. *124*, 679–683.

38. Anastasiadis, P.Z., Moon, S.Y., Thoreson, M.A., Mariner, D.J., Crawford, H.C., Zheng, Y., and Reynolds, A.B. (2000). Inhibition of RhoA by p120 catenin. Nat. Cell Biol. *2*, 637–644.

39. Wildenberg, G.A., Dohn, M.R., Carnahan, R.H., Davis, M.A., Lobdell, N.A., Settleman, J., and Reynolds, A.B. (2006). p120-catenin and p190RhoGAP regulate cell-cell adhesion by coordinating antagonism between Rac and Rho. Cell *127*, 1027–1039.

40. Piekny, A.J., and Glotzer, M. (2008). Anillin is a scaffold protein that links RhoA, actin, and myosin during cytokinesis. Curr. Biol. *18*, 30–36.

41. Priya, R., Gomez, G.A., Budnar, S., Verma, S., Cox, H.L., Hamilton, N.A., and Yap, A.S. (2015). Feedback regulation through myosin II confers robustness on RhoA signalling at E-cadherin junctions. Nat. Cell Biol. *17*, 1282–1293.

42. Takesono, A., Moger, J., Farooq, S., Cartwright, E., Dawid, I.B., Wilson, S.W., and Kudoh, T. (2012). Solute carrier family 3 member 2 (Slc3a2) controls yolk syncytial layer (YSL) formation by regulating microtubule networks in the zebrafish embryo. Proc. Natl. Acad. Sci. USA *109*, 3371–3376.

43. Schwayer, C., Shamipour, S., Pranjic-Ferscha, K., Schauer, A., Balda, M., Tada, M., Matter, K., and Heisenberg, C.-P. (2019). Mechanosensation of tight junctions depends on ZO-1 phase separation and flow. Cell *179*, 937–952.e18.

44. Liu, Y.-J., Le Berre, M., Lautenschlaeger, F., Maiuri, P., Callan-Jones, A., Heuzé, M., Takaki, T., Voituriez, R., and Piel, M. (2015). Confinement and low adhesion induce fast amoeboid migration of slow mesenchymal cells. Cell *160*, 659–672.

45. Ruprecht, V., Wieser, S., Callan-Jones, A., Smutny, M., Morita, H., Sako, K., Barone, V., Ritsch-Marte, M., Sixt, M., Voituriez, R., et al. (2015). Cortical contractility triggers a stochastic switch to fast amoeboid cell motility. Cell *160*, 673–685.

46. Munro, E., Nance, J., and Priess, J.R. (2004). Cortical flows powered by asymmetrical contraction transport PAR proteins to establish and maintain anterior-posterior polarity in the early C. elegans embryo. Dev. Cell *7*, 413–424.

47. Mayer, M., Depken, M., Bois, J.S., Jülicher, F., and Grill, S.W. (2010). Anisotropies in cortical tension reveal the physical basis of polarizing cortical flows. Nature *467*, 617–621.

48. Hannezo, E., and Heisenberg, C.-P. (2019). Mechanochemical feedback loops in development and disease. Cell *178*, 12–25.

49. Levayer, R., and Lecuit, T. (2012). Biomechanical regulation of contractility: spatial control and dynamics. Trends Cell Biol. *22*, 61–81.

50. Képiró, M., Várkuti, B.H., Végner, L., Vörös, G., Hegyi, G., Varga, M., and Málnási-Csizmadia, A. (2014). para-Nitroblebbistatin, the non-cytotoxic and photostable myosin II inhibitor. Angew. Chem. Int. Ed. Engl. *53*, 8211–8215.

51. Jayashankar, V., Nguyen, M.J., Carr, B.W., Zheng, D.C., Rosales, J.B., Rosales, J.B., and Weiser, D.C. (2013). Protein phosphatase 1 β paralogs encode the zebrafish myosin phosphatase catalytic subunit. PLoS One *8*, e75766.

52. Kametani, Y., and Takeichi, M. (2007). Basal-to-apical cadherin flow at cell junctions. Nat. Cell Biol. *9*, 92–98.

53. Peglion, F., Llense, F., and Etienne-Manneville, S. (2014). Adherens junction treadmilling during collective migration. Nat. Cell Biol. *16*, 639–651.

54. Hong, S., Troyanovsky, R.B., and Troyanovsky, S.M. (2013). Binding to F-actin guides cadherin cluster assembly, stability, and movement. J. Cell Biol. *201*, 131–143.

55. Hannezo, E., Dong, B., Recho, P., Joanny, J.-F., and Hayashi, S. (2015). Cortical instability drives periodic supracellular actin pattern formation in epithelial tubes. Proc. Natl. Acad. Sci. USA *112*, 8620–8625.

56. Sonal, K.A., Ganzinger, K.A., Vogel, S.K., Mücksch, J., Blumhardt, P., and Schwille, P. (2018). Myosin-II activity generates a dynamic steady state with continuous actin turnover in a minimal actin cortex. J. Cell Sci. *132*, jcs219899.

57. Charras, G.T., Hu, C.-K., Coughlin, M., and Mitchison, T.J. (2006). Reassembly of contractile actin cortex in cell blebs. J. Cell Biol. *175*, 477–490.

58. Diz-Muñoz, A., Romanczuk, P., Yu, W., Bergert, M., Ivanovitch, K., Salbreux, G., Heisenberg, C.P., and Paluch, E.K. (2016). Steering cell migration by alternating blebs and actin-rich protrusions. BMC Biol. *14*, 74.

59. Bois, J.S., Jülicher, F., and Grill, S.W. (2011). Pattern formation in active fluids. Phys. Rev. Lett. *106*, 028103.

60. Noren, N.K., Arthur, W.T., and Burridge, K. (2003). Cadherin engagement inhibits RhoA via p190RhoGAP. J. Biol. Chem. *278*, 13615–13618.

61. Smith, A.L., Dohn, M.R., Brown, M.V., and Reynolds, A.B. (2012). Association of Rho-associated protein kinase 1 with E-cadherin complexes is mediated by p120-catenin. Mol. Biol. Cell *23*, 99–110.

62. Tabdanov, E., Borghi, N., Brochard-Wyart, F., Dufour, S., and Thiery, J.-P. (2009). Role of E-cadherin in membrane-cortex interaction probed by nanotube extrusion. Biophys. J. *96*, 2457–2465.

63. Mangeol, P., Massey-Harroche, D., Bivic, A.L., and Lenne, P.-F. (2019). Nectins Rather than E-Cadherin Anchor the Actin Belts at Cell-Cell Junctions of Epithelia (Cell Biology).

64. Terry, S.J., Zihni, C., Elbediwy, A., Vitiello, E., Leefa Chong San, I.V., Balda, M.S., and Matter, K. (2011). Spatially restricted activation of RhoA signalling at epithelial junctions by p114RhoGEF drives junction formation and morphogenesis. Nat. Cell Biol. *13*, 159–166.

65. Kaizuka, Y., Douglass, A.D., Varma, R., Dustin, M.L., and Vale, R.D. (2007). Mechanisms for segregating T cell receptor and adhesion molecules during immunological synapse formation in Jurkat T cells. Proc. Natl. Acad. Sci. USA *104*, 20296–20301.

66. Hartman, N.C., Nye, J.A., and Groves, J.T. (2009). Cluster size regulates protein sorting in the immunological synapse. Proc. Natl. Acad. Sci. USA *106*, 12729–12734.

67. Pal, D., Ellis, A., Sepúlveda-Ramírez, S.P., Salgado, T., Terrazas, I., Reyes, G., De La Rosa, R., Henson, J.H., and Shuster, C.B. (2020). Rac and Arp2/3-nucleated actin networks antagonize Rho during mitotic and meiotic cleavages. Front. Cell Dev. Biol. *8*, 591141.

68. Belardi, B., Son, S., Felce, J.H., Dustin, M.L., and Fletcher, D.A. (2020). Cell–cell interfaces as specialized compartments directing cell function. Nat. Rev. Mol. Cell Biol. *21*, 750–764.

69. Diz-Muñoz, A., Krieg, M., Bergert, M., Ibarlucea-Benitez, I., Muller, D.J., Paluch, E., and Heisenberg, C.-P. (2010). Control of directed cell migration in vivo by membrane-to-cortex attachment. PLoS Biol. *8*, e1000544.

70. Wu, S.K., Gomez, G.A., Michael, M., Verma, S., Cox, H.L., Lefevre, J.G., Parton, R.G., Hamilton, N.A., Neufeld, Z., and Yap, A.S. (2014). Cortical F-actin stabilization generates apical–lateral patterns of junctional contractility that integrate cells into epithelia. Nat. Cell Biol. *16*, 167–178.

71. Hong, S., Troyanovsky, R.B., and Troyanovsky, S.M. (2010). Spontaneous assembly and active disassembly balance adherens junction homeostasis. Proc. Natl. Acad. Sci. USA *107*, 3528–3533.

72. Noordstra, I., Hermoso, M.D., Schimmel, L., Bonfim-Melo, A., Currin-Ross, D., Duong, C.N., Kalappurakkal, J.M., Morris, R.G., Vestweber, D., Mayor, S., et al. (2023). An E-cadherin-actin clutch translates the mechanical force of cortical flow for cell-cell contact to inhibit epithelial cell locomotion. Dev. Cell *58*, 1748–1763.e6.

73. Xiong, F., Tentner, A.R., Huang, P., Gelas, A., Mosaliganti, K.R., Souhait, L., Rannou, N., Swinburne, I.A., Obholzer, N.D., Cowgill, P.D., et al. (2013). Specified neural progenitors sort to form sharp domains after noisy shh signaling. Cell *153*, 550–561.

74. Kardash, E., Reichman-Fried, M., Maître, J.-L., Boldajipour, B., Papusheva, E., Messerschmidt, E.-M., Heisenberg, C.-P., and Raz, E. (2010). A role for Rho GTPases and cell-cell adhesion in single-cell motility *in vivo*. Nat. Cell Biol. *12*, 47–53.

75. Iioka, H., Ueno, N., and Kinoshita, N. (2004). Essential role of MARCKS in cortical actin dynamics during gastrulation movements. J. Cell Biol. *164*, 169–174.

76. Schindelin, J., Arganda-Carreras, I., Frise, E., Kaynig, V., Longair, M., Pietzsch, T., Preibisch, S., Rueden, C., Saalfeld, S., Schmid, B., et al. (2012). Fiji: an open-source platform for biological-image analysis. Nat. Methods *9*, 676–682.

77. Sommer, C., Straehle, C., Köthe, U., and Hamprecht, F.A. (2011). Ilastik: interactive learning and segmentation toolkit. In 2011 IEEE International Symposium on Biomedical Imaging: From Nano to Macro, pp. 230–233.

78. Jakobs, M.A.H., Dimitracopoulos, A., and Franze, K. (2019). KymoButler, a deep learning software for automated kymograph analysis. eLife *8*, e42288.

79. Xu, T., Vavylonis, D., Tsai, F.-C., Koenderink, G.H., Nie, W., Yusuf, E., Lee, I.-J., Wu, J.-Q., and Huang, X. (2015). SOAX: A software for quantification of 3D biopolymer networks. Sci. Rep. *5*, 9081.

80. Westerfield, M. (2000). The zebrafish book: A guide for the laboratory use of zebrafish. http://zfin.org/zf_info/zfbook/zfbk.html.

81. Kimmel, C.B., Ballard, W.W., Kimmel, S.R., Ullmann, B., and Schilling, T.F. (1995). Stages of embryonic development of the zebrafish. Dev. Dyn. *203*, 253–310.

82. Harrison, O.J., Brasch, J., Katsamba, P.S., Ahlsen, G., Noble, A.J., Dan, H., Sampogna, R.V., Potter, C.S., Carragher, B., Honig, B., et al. (2020). Family-wide structural and biophysical analysis of binding interactions among non-clustered δ-protocadherins. Cell Rep. *30*, 2655–2671.e7.

83. Sakaue-Sawano, A., Kurokawa, H., Morimura, T., Hanyu, A., Hama, H., Osawa, H., Kashiwagi, S., Fukami, K., Miyata, T., Miyoshi, H., et al. (2008). Visualizing spatiotemporal dynamics of multicellular cell-cycle progression. Cell *132*, 487–498.

84. Reversat, A., Gaertner, F., Merrin, J., Stopp, J., Tasciyan, S., Aguilera, J., de Vries, I., Hauschild, R., Hons, M., Piel, M., et al. (2020). Cellular locomotion using environmental topography. Nature *582*, 582–585.

85. Tinevez, J.-Y., Perry, N., Schindelin, J., Hoopes, G.M., Reynolds, G.D., Laplantine, E., Bednarek, S.Y., Shorte, S.L., and Eliceiri, K.W. (2017). TrackMate: an open and extensible platform for single-particle tracking. Methods *115*, 80–90.

86. Jönsson, P., Jonsson, M.P., Tegenfeldt, J.O., and Höök, F. (2008). A method improving the accuracy of fluorescence recovery after photobleaching analysis. Biophys. J. *95*, 5334–5348.

87. Goldman, R.D., Swedlow, J.R., and Spector, D.L. (2005). Live Cell Imaging: A Laboratory Manual, Second Edition (CSH Press).

88. Mahlandt, E.K., Arts, J.J.G., van der Meer, W.J., van der Linden, F.H., Tol, S., van Buul, J.D., Gadella, T.W.J., and Goedhart, J. (2021). Visualizing endogenous Rho activity with an improved localization-based, genetically encoded biosensor. J. Cell Sci. *134*, jcs258823.

89. Manders, E.M.M., Verbeek, F.J., and Aten, J.A. (1993). Measurement of co-localization of objects in dual-colour confocal images. J. Microsc. *169*, 375–382.

90. Nunez-Iglesias, J., Blanch, A.J., Looker, O., Dixon, M.W., and Tilley, L. (2018). A new Python library to analyse skeleton images confirms malaria parasite remodelling of the red blood cell membrane skeleton. PeerJ *6*, e4312.

91. Baranova, N., and Loose, M. (2017). Chapter 21. Single-molecule measurements to study polymerization dynamics of FtsZ-FtsA copolymers. In Methods in Cell Biology Cytokinesis, A. Echard, ed. (Academic Press), pp. 355–370.

92. Gebhardt, J.C.M., Suter, D.M., Roy, R., Zhao, Z.W., Chapman, A.R., Basu, S., Maniatis, T., and Xie, X.S. (2013). Single-molecule imaging of transcription factor binding to DNA in live mammalian cells. Nat. Methods *10*, 421–426.

93. Barberi, L., and Kruse, K. (2022). Localized states in active fluids. Preprint at arXiv. https://arxiv.org/abs/2209.02581.

STAR★METHODS

KEY RESOURCES TABLE

REAGENT or RESOURCE	SOURCE	IDENTIFIER
Antibodies		
zebrafish E-cadherin antibody produced in rabbit	Maître et al.[20]	N/A
peroxidase AffiniPure goat anti-rabbit IgG (H+L)	Jackson ImmunoResearch	Cat#111-035-003; RRID: AB_2313567
Chemicals, peptides, and recombinant proteins		
zebrafish E-cadherin ectodomain with 12x His-tag	This study	N/A
FreeStyle 293 Expression Medium	Gibco	Cat#12338018
Polyethylenimine, Linear, MW 25000	Polysciences	Cat#23966
Opti-MEM Reduced Serum Medium	Gibco	Cat#31985062
Sulfo-cyanine5-maleimide	Lumiprobe	Cat#13380
DMEM/F-12	Gibco	Cat#11320033
GlutaMAX Supplement	Gibco	Cat#35050061
Penicillin-Streptomycin	Gibco	Cat#15070063
Actin protein (rhodamine) from rabbit skeletal muscle	Cytoskeleton, Inc.	Cat#AR05-B
para-nitro-Blebbistatin	Képiró et al.[50]; Cayman Chemical	Cat#24171
1-Oleoyl lysophosphatidic acid sodium salt	Tocris Bioscience	Cat#3854
SYLGARD® 184 PDMS	Merck	Cat#761036
18:1 (Δ9-Cis) PC (DOPC)	Avanti polar lipids	Cat#850375C
18:1 DGS-NTA	Avanti polar lipids	Cat#790528
DSPE-PEG(2000) Amine	Avanti polar lipids	Cat#880128
Critical commercial assays		
mMESSAGE mMACHINE SP6 Transcription Kit	Invitrogen	Cat#AM1340
Gibson Assembly Cloning Kit	NEB	Cat#E5510S
Gateway Cloning Kit	Invitrogen	Cat#11791020; Cat#11789020
Experimental models: Cell lines		
FreeStyle 293-F Cells	Gibco	Cat#R79007; RRID: CVCL_D603
Experimental models: Organisms/strains		
Zebrafish: wildtype ABxTL	MPI-CBG	ZDB-GENO-031202-1
Zebrafish: Tg(cdh1-tdTomato)xt18	Cronan and Tobin[31]	ZDB-FISH-201125-9
Zebrafish: Tg(cdh1-mlanYFP)xt17	Cronan and Tobin[31]	ZDB-FISH-201125-8
Zebrafish: Tg(actb2:HA-mCherry2)	Xiong et al.[73]	ZDB-TGCONSTRCT-130625-1
Zebrafish: Tg(actb2:Myl12.1-eGFP;actb2:Utrophin-mCherry)	This study	N/A
Oligonucleotides		
Morpholino: MO-cdh1 TAAATCGCAGCTCTTCCTTCCAACG	Babb and Marrs.[30]; Gene Tools	ZDB-MRPHLNO-050421-2
Primers: EcadΔcyto-GFP Forward: GATCTCGAGGTGTCCAAAGGCG	This study; Microsynth	N/A
Primers: EcadΔcyto-GFP Reverse: CAGCAGAGGCTCTTTCTTGCTG	This study; Microsynth	N/A
Primers: GFP-AHPH-WT Forward: GCAGGATCCCATCGATTATGGTGAGCAAGGGCGA	This study; Microsynth	N/A
Primers: GFP-AHPH-WT Reverse: CGTAATACG ACTCACTATAGTTTCAAGGCTTTCCA ATAGGTTTGTAGCAA	This study; Microsynth	N/A
Primers: mCherry-AHPH-WT Forward: GCTGTACAAGTCCGGACTCAGATCTCGAGC	This study; Microsynth	N/A
Primers: mCherry-AHPH-WT Reverse: TGAGTCCGGACTTGTACAGCTCGTCCATGCCG	This study; Microsynth	N/A

Continued

REAGENT or RESOURCE	SOURCE	IDENTIFIER
Primers: GFP-AHPH-DM Forward: AATACAAGCTA CTTGTTCTTTTTGCAGGATCCCATCGA TTATGGTGAGCAAGGGCGAG	This study; Microsynth	N/A
Primers: GFP-AHPH-DM Reverse: TCTGGATCTACG TAATACGACTCACTATAGTTCTAGAGGCTCAAGGC TTTCCAATAGGTTTGTAGC	This study; Microsynth	N/A
gBlocks gene fragment: Ftractin ACAAGT TTGTACAAAAAAGCAGGCTTCGGATCCATG GCGCGTCCGAGAGGAGCTGGCCCGTGCT CACCTGGTCTCGAAAGGGCTCCACGGCG GAGCGTAGGTGAGTTGAGACTTTTGTTTGA AGCACGATGCGCTGCGGTCGCTGCTGCTG CTGCAGCTGGGGGGCTAGCGCTACCGCTC GAGGACCCAGCTTTCTTGTACAAAGTGGGa	IDT	N/A
Recombinant DNA		
pcDNA3.1(-)-EcadECD (zebrafish)	This study	N/A
pEGFP-RhoA Biosensor	Piekny and Glotzer[40]	Addgene #68026
GFP-AHPH-DM	Priya et al.[41]	Addgene #71368
PCS2-GFP-AHPH-WT	This study	N/A
PCS2-GFP-AHPH-DM	This study	N/A
PCS2-mCherry-AHPH-WT	This study	N/A
PCS2-Ftractin-GFP	This study	N/A
PCS2-Ftractin-mKO2	This study	N/A
PCS2-E-cadherin-GFP(zebrafish)	Kardash et al.[74]	N/A
PCS2-EcadΔcyto-GFP	This study	N/A
PCS2-lefty1	Maître et al.[20]	N/A
PCS2-membrane-RFP	Iioka et al.[75]	N/A
PCS2-CA-Mypt	Jayashankar et al.[51]	N/A
PCS2-CA-RhoA	Takesono et al.[42]	N/A
PCS2-CA-Ezrin2	Diz-Muñoz et al.[58]	N/A
Software and algorithms		
Fiji	Schindelin et al.[76]	https://fiji.sc/
MATLAB R2017b	The MathWorks, Inc	https://mathworks.com/products/matlab.html
Python 3.6	Python Software Foundation	https://www.python.org
ILASTIK	Sommer et al.[77]	https://www.ilastik.org
KymoButler	Jakobs et al.[78]	https://github.com/elifesciences-publications/KymoButler
SOAX	Xu et al.[79]	https://www.lehigh.edu/~div206/soax/
Prism 6	GraphPad	https://www.graphpad.com/scientific-software/prism/
Inkscape	Inkscape Project (2000)	https://inkscape.org
Other		
HisTrap Fast Flow Crude column	Cytiva	Cat#GE29-0486-31
PD-10 desalting columns	Cytiva	Cat#17085101
Zeba Spin Desalting Columns 7K MWCO	Thermo Scientific	Cat#89882

RESOURCE AVAILABILITY

Lead contact
Further information and requests for resources and reagents should be directed to and will be fulfilled by the lead contact, Carl-Philipp Heisenberg (heisenberg@ist.ac.at).

Materials availability
Plasmids generated in this study are available from the lead contact upon request.

Data and code availability

- All original microscopy data any additional information reported in this paper is available from the lead contact upon request.
- All original code is available from the lead contact upon request.
- Any additional information required to reanalyze the data reported in this paper is available from the lead contact upon request.

EXPERIMENTAL MODEL DETAILS

Zebrafish husbandry and strains
Zebrafish (*Danio rerio*) were housed in 28°C water (pH 7.5 and conductivity 400 μS) under a 14 h light/10 h dark cycle.[80] Embryos were raised at 28.5–31°C in E3 medium and staged as previously described.[81] The following lines were used: WT ABxTL, *Tg(cdh1-tdTomato)xt18*,[31] *Tg(cdh1-mlanYFP)xt17*,[31] *Tg(actb2:HA-mCherry2)*[73] and *Tg(actb2:Myl12.1-eGFP;actb2:Utrophin-mCherry)* generated by crossing the preexisting lines *Tg(actb2:Myl12.1-eGFP)* and *Tg(actb2:Utrophin-mCherry)*.[20,35] Fish husbandry and breeding were done in the aquatics facility of IST Austria according to local regulations, and all procedures were approved by the Ethics Committee of IST Austria regulating animal care and usage.

Zebrafish primary cell cultures
30 min before live imaging, embryos were transferred to pre-warmed (28.5–31°C) 0.9x DMEM/F12 medium[22] supplemented with GlutaMAX and Penicillin-Streptavidin. The blastoderm caps were dissected from the yolk cells at sphere stage with forceps and transferred to 1.5 ml eppendorf tubes using glass pipettes. In the case of inhibitor use, media in the eppendorfs was exchanged to inhibitor-containing media 10 min before cell seeding. All explants were dissociated by gentle tapping and seeded on bilayers covered with control or inhibitor-supplemented media at 29°C.

METHOD DETAILS

Expression and purification of EcadECD
cDNA encoding the zebrafish E-cadherin ectodomain (Q90Z37_DANRE, EC1 to EC5, residues G141 to D672), with an N-terminal human CD33 signaling peptide and C-terminal 12xHis purification tag was codon optimized and ordered as a gBlocks Gene Fragment (IDT) with overhangs for Gibson assembly. The sequence was engineered to have a single Cys in the EC5 domain for site-specific labeling as previously described.[27] The product was inserted between EcoRI and XbaI sites of pcDNA3.1(-) mammalian expression vector. EcadECD was expressed in suspension FreeStyle 293-F cells in Freestyle 293 Expression Medium at 37°C with 8% CO_2. FreeStyle 293-F cells were transiently transfected using polyethyleneimine in Opti-MEM Reduced Serum Medium. Cultures were supplemented with 5 mM $CaCl_2$ 2 days after transfection,[82] and culture media containing secreted EcadECD was collected 5 days later. Filtered and conditioned media was loaded to HisTrap Fast Flow Crude Column for affinity chromatography on an ÄKTA Pure Fast Protein Liquid Chromatography system (Cytiva) and eluted with an imidazole gradient at 4°C. Clean fractions, determined by SDS-PAGE stained with Coomassie Brilliant Blue (Figure S1A), were pooled together and dialyzed overnight in storage solution (100 mM NaCl, 20 mM Tris-Cl pH 8, 3 mM $CaCl_2$). Alternatively, the buffer was exchanged using PD-10 desalting columns. The identity of the protein was verified with N-terminal sequencing. Clean protein was aliquoted at a final 50 μg/ml concentration and snap-frozen for long-term storage at -80°C with 5% glycerol.

Fluorescent labeling of EcadECD
To perform FRAP experiments for determining the protein diffusion constant, EcadECD was labeled at the Cys residue using Sulfo-C5-maleimide. First, the sample was incubated for 20 min with TCEP (100 molar fold excess of protein) at room temperature. Then, maleimide dye (10 molar fold excess of protein) was added to the sample and incubated at room temperature for 1 h. Excess dye was removed using a 7K MWCO Zeba™ Spin Desalting Column.

Western blot
Eluted protein fraction was incubated at 70°C in NuPAGE LDS Sample Buffer (Invitrogen) and NuPAGE Sample Reducing Agent for 10 min before getting loaded to a 4-12% NuPAGE Bis-Tris protein gel. After SDS-PAGE, proteins were transferred to a membrane

using the iBlot Western Blotting System (Thermo Fisher Scientific) according to the manufacturer's protocol. For the immunodetection of EcadECD, membrane was blocked with blocking buffer (3% BSA, 0.2% Tween-20 in PBS) for 1 h at room temperature and incubated overnight with rabbit anti-zebrafish Ecad antibody[20] (1:5000) in blocking solution. After 3x10 min washes with PBT (PBS with 0.2% Tween), membrane was incubated with Peroxidase AffiniPure Goat Anti-Rabbit IgG (H+L) (1:20000) for 45 min at room temperature and washed 4x5 min with PBT, then 2x5 min with PBS. The membrane was developed with Clarity Western ECL Substrate (Biorad) before imaging.

Preparation of SLBs and functionalization with EcadECD
To make small unilamellar vesicles, 1,2-dioleoyl-sn-glycero-3-phosphocholine (DOPC), 1,2-dioleoyl-sn-glycero-3-[(N-(5-amino-1-carboxypentyl)iminodiacetic acid)succinyl] (nickel salt, Ni-NTA-DOGS), 1,2-distearoyl-sn-glycero-3-phosphoethanolamine-N-[amino(polyethylene glycol)-2000] (DSPE-PEG2000), and freshly dissolved cholesterol lipid mixtures in chloroform with a molar ratio of 55.9:4:0.1:40 (unless otherwise stated) were prepared in glass vials and evaporated under N_2 stream to get a homogenous thin film. Lipids were further vacuumed for 1 h to remove the remaining solvent and frozen at -20°C unless freshly used. Lipid films were resuspended in vesicle buffer (75 mM NaCl, 20 mM Hepes) at 37°C by vortexing to a final concentration of 1.5mM and freeze-thawed in liquid nitrogen 5x before aliquoting. Aliquots were kept at -20°C and used within 2 weeks. For experiments, solutions were diluted to 0.2 mM with vesicle buffer and bath sonicated for 15 min.

To form the lipid bilayers on coverslips, 24×50 mm high-precision coverslips were cleaned in Piranha solution (3:1, 98% H_2SO_4:30% H_2O_2) for 1 h. The coverslips were further washed with deionized water and kept in water to be used within 2 weeks. Before use, coverslips were dried, PCR tubes, with their conical ends removed, were attached to the coverslips as reaction chambers, using ultraviolet curing glue (Norland 63) under UV light for 5 min. The coverslips were then treated in a Zepto B plasma oven (Diener Electronic) for 12 min at 30 W under 1 L/h airflow. Immediately after, vesicle mixtures were added to reaction chambers, and after letting the vesicles settle for 4 min, 3 mM $CaCl_2$ was added to enhance vesicle fusion on the activated surface. Chambers were incubated for 1 h at 37°C, washed with PBS through serial washes by vigorous pipetting and incubated with 0.1% fatty acid-free BSA in protein storage buffer for 30 min. EcadECD was added to a 2 μg/ml final concentration to these chambers and incubated for 45 min at room temperature before changing to pre-warmed imaging medium with serial washes.

Cloning of expression constructs
PCR products from plasmids GFP-AHPH-WT[40] (a gift from Michael Glotzer) and GFP-AHPH-DM[41] (a gift from Alpha Yap) were subcloned to create PCS2-GFP-AHPH-WT and PCS2-GFP-AHPH-DM plasmids with Gateway cloning. cDNA sequence coding for Ftractin (IP3KA_RAT, residues M10 to G52) was codon-optimized and ordered as a gBlocks Gene Fragment to create PCS2-Ftractin-GFP and PCS2-Ftractin-mKO2 plasmids. All products were cloned with attB arms and recombined with pDONR221 (P1-P2)(Lawson#208) to create entry clones, and further recombined with p3E-mNeonGreen (Allelebiotech), p3E-mKO2,[83] p3E-polyA (Chien#302), and pCS-Dest2 (Lawson #444) to create expression plasmids. PCS2-mCherry-AHPH-WT was created by replacing PCS2-GFP-AHPH-WT plasmid's GFP sequence with mCherry using Gibson assembly. Ecad lacking its cytoplasmic domain (EcadΔcyto-GFP) was subcloned from full-length E-cadherin-GFP plasmid (a gift from Erez Raz).[74]

Embryo microinjections
All embryos were microinjected with 100 pg *lefty1* mRNA at 1-cell stage to induce ectoderm fate. To visualize cell membrane, F-actin and RhoA activities, and to modulate contractility and cortex-to-membrane attachment, following mRNAs were additionally injected into 1-cell stage embryos: 80 pg *membrane-RFP*,[75] 60pg *Ftractin-mNeonGreen*, 60 pg of *Ftractin-mKO2*, 80 pg of *GFP-AHPH-WT*,[40] 100 pg of mCherry-AHPH-WT, 80 pg of *GFP-AHPH-DM*,[41] 200 pg of *EcadΔcyto-GFP*, 70 pg *constitutively active Myosin Phosphatase (CA-Mypt)*,[51] 3 pg *constitutively active RhoA (CA-RhoA)*[42] and 200 pg *constitutively active Ezrin2 (CA-Ezrin2 T564D)*.[58] To decrease endogenous Ecad amounts, 2 ng *cdh1* morpholino[30] was injected at 1-cell stage. Additionally, to visualize F-actin, 0.125 ng Actin protein from rabbit skeletal muscle labeled with TRITC was injected to 1-cell stage embryos. Synthetic mRNAs were produced using the SP6 mMessage mMachine kit and Actin protein was handled according to the manufacturer's protocol.

Inhibitor treatments
The following inhibitor concentrations in DMEM/F12 media were used: 10 μM for para-nitroblebbistatin (10 mM stock dissolved in DMSO) and 20 nM for 1-Oleoyl lysophosphatidic acid sodium salt (LPA) (5 mM stock dissolved in water). As controls, DMEM/F12 media with or without DMSO (0.1%) were used depending on the solvent of the pharmacological inhibitors.

Cell confinement by polydimethylsiloxane (PDMS) confiners
In the case of bilayers without EcadECD (except for adherence assay, see below), cells were put under slight PDMS confinement to increase the imaged contact area. Cells were seeded onto bilayers formed on coverslips glued to the bottom of plastic dishes containing a 17 mm round hole, on which a chamber was created by glueing a ring cut from a 15 ml falcon tube. 1:10 PDMS mixtures were prepared as previously described,[84] degassed for 2 min at 2,000 rpm (mix) and for 2 min at 2,200 rpm (defoam) in a mixer/defoamer (ARE-250, Thinky). PDMS was poured onto a wafer and 10 mm round coverslips that were activated by plasma cleaning were pressed onto this mix. The wafer was baked at 95 °C for 15 min and the 16 μm high micropillar-coated coverslips were gently

removed from the wafer to be used as confiners. Before use, a confiner was incubated for 5 min with FBS, washed with PBS and kept in culture medium. For imaging, the confiner was placed on a soft pillar attached to a magnetic glass lid, closed on the cells, and kept in place using a magnetic ring underneath the dish during imaging.

Microscopy

Imaging was performed using microscopes with heating chambers at 29°C. For imaging contact formation, acquisition was started as soon as cells were seeded. For imaging steady contacts, cells were imaged 10-30 min post-seeding. Cultures were kept for $\sim$ 2 h maximum, and dividing or apoptotic cells were excluded from the subsequent analysis. Most contacts were imaged using an LSM800 equipped with an Airyscan detector and a Plan-APOCHROMAT 63x/1.4 oil objective and z-position was manually adjusted during time-lapse acquisition. To quantify intensity changes during time-lapse imaging of Ecad and RhoA biosensors, which showed weaker signal and/or higher photobleaching, Andor Dragonfly 505 equipped with 1x Andor Zyla sCMOS detector and a CFI Apochromat TIRF 60x/NA 1.49/WD 0.13 mm oil objective was used with Perfect Focus. For all markers, imaging parameters that minimized photobleaching were used for time-lapse analysis (Figure S2I). For determining the number of cells on bilayers and imaging cell doublets, Plan-Apochromat 10x/0.45 and Plan Apochromat 20x/0.8 objectives, respectively, were used on the LSM800. For imaging bilayers, single molecules and FRAP experiments, A TILL Photonics iMic TIRF System equipped with Andor TuCam detection and a 100x/1.49 oil objective was used. For UV laser ablations, A Nikon CSU-W1 spinning disk microscope equipped with a CFI Plan Apo VC 60x WI/NA 1.2 /WD 0.28-0.31 mm water objective and 355 nm pulsed laser was used.

Data visualization and analysis

All micrographs for figures were adjusted for contrast using Fiji.[76] Data for the rest of the analysis were processed raw. Data were plotted using Graphpad Prism 6. For sketches and final formatting of figures, Inkscape was used.

In Videos S2 and S3, frame averages were made over 2 subsequent frames for better visualization. Temporal visualization in Video S2 was performed with the Temporal-Color Code plugin in Fiji. Temporal trajectory construction in Video S3 was performed with the TrackMate plugin[85] in Fiji, based on a Gaussian fit with an estimated diameter of 0.5 μm. Linking distance of a maximum of 0.3 μm and gaps of a maximum of 3 frames were allowed to account for failures to detect Ecad clusters. Trajectories longer than 1 min were shown in the movie.

FRAP experiments and analysis

To measure the diffusion constant of EcadECD-Cy5 on different bilayer compositions, photobleaching experiments were performed with a frame rate of 2 s per frame. 5 pre-bleach frames were acquired, followed by photobleaching of an area of about 10 μm × 10 μm. Recovery of the signal was analyzed using the frap_analysis program[86] implemented in MATLAB.

FRAP experiments for cellular Ecad were performed using cells obtained from *Tg(cdh1:mlanYFP)* embryos, with a frame rate of 0.5 s per frame. 5 pre-bleach frames were acquired, followed by photobleaching of an area of about 5 μm × 5 μm at the cell contact. A photobleach correction due to the imaging process was performed using an unbleached area of the contact, and the photobleach curve was normalized to the first pre-bleach data point. To obtain the recovery times and immobile fractions, monoexponential functions were fitted to the recovery curves.[87]

Quantification of adherence

To check for the specificity of cell-bilayer adhesions, either bilayers were prepared without EcadECD or Ecad was knocked down in cells using *cdh1* morpholino. Cells in bright-field images of the same ROI were counted before and after washing off the chambers by exchanging media once. Remaining cells on the bilayers were considered adherent.

Analysis of Ecad, GTP-RhoA, cell membrane, and *F*-actin average intensities and Myosin-2 mini-filament density

Contact intensity was measured using a custom Python script, by taking ratios of background intensity-subtracted total intensity to total area determined by local thresholding. Contact radii were estimated from the segmented contact areas, assuming that contacts were generally circular. For rim-to-center ratios, a distance equal to 20% of the radius from the edge was defined as the contact rim and the rest as the contact center. For measurements over time, intensity values measured in each time-lapse were first normalized to the maximum intensity in that movie to remove injection-based variations between samples. Out-of-focus frames in Airsycan movies were excluded from time-lapse intensity analysis (Video S1).

AHPH expression was detected both diffusely throughout the contact and as cortical foci. These foci were homogeneously distributed at the adhesion-free interface (Figure S2A), and once the contact area stabilized, preferentially localized to the contact rim (Figure 1B). Given that such foci were not found using other RhoA biosensors,[88] they were excluded from the average intensity analysis.

To detect Myosin-2 mini-filaments ILASTIK was used.[77] Percentages of total area positive for Myosin-2 signal in the segmented images were determined using a custom Python script.

Analysis of cross-correlation

Time-lapse movies of Myosin-2 were segmented in ILASTIK to calculate the area covered by Myosin-2 mini-filaments and the entire contact area or the area covered by blebs as a function of time. To calculate the linear correlation between Myosin-2 density and

contact area or Myosin-2 density and bleb area as a function of lag time, the Correlation function of Origin(Pro) was used on paired data from single cells and the auto-covariance at zero lag was normalized to 1.

Analysis of colocalization and peaks of signal intensities at the contact rim
Dual-color Airyscan images were used for colocalization analysis. Images were analyzed using Coloc 2 plugin in Fiji with Cortes' automatic thresholding. Manders' coefficients M1 and M2 (0 to 1), which give a fraction of overlap between positive pixels, and Pearson's correlation coefficient (-1 to 1), which gives a value based on the correlation of intensities at two channels, were calculated.[89] In order to visualize the colocalization, intensity profiles over a 0.3 μm-thick line perpendicular to the rim were plotted together for both channels. Distances to the peak of F-actin signal at the rim, from peaks of GTP-RhoA, Myosin-2 and Ecad signals were calculated from such profiles.

Plotting radial intensity profiles
An Airsycan image of a roughly circular contact was rotated 1° at a time using the transform function in Fiji and the resulting 360 rotated images were averaged to create an average radial intensity image. Radial intensity was calculated along a line crossing the contact diameter of this image. For plotting radial profiles from multiple cells, profiles were first normalized to contact length, and then to average intensity.

Analysis of *F*-actin and Ecad flows
Time-lapse images of Ftractin-mNeonGreen- or Ecad-mlanYFP-expressing cells were used for flow analysis. Unless specified, mature contacts (>10 min post contact initiation) were used for analysis to rule out contact expansion effects and retracting protrusions at the contact rim were excluded from analysis. The built-in Fiji function Multi Kymograph was used to get kymographs along each cell's diameter. The motion of fluorescent particles within those kymographs was detected using KymoButler, a deep learning automated kymograph analysis software[78] in Mathematica 12.1. BiKymoButler function was used to detect bidirectional tracks with a particle size of 0.3 μm and a minimum duration of 10 s. From these tracks, location and net velocity of particle movements with respect to the center of mass and track durations were calculated. For radial velocities along the contact, multiple kymographs were made with 10° rotations around the center of mass, and net velocities were plotted against their distance from the center of mass. For analysis of flows around LPA-induced ectopic foci, kymographs of ~6 μm in length, were constructed around the foci. The net velocity of particle movements was calculated with respect to foci position. For local analysis of flows towards blebs, kymographs were generated from the contact midpoint towards the rim location where a bleb retracts, encompassing a period of 30 s before to 30 s after the bleb retraction was completed. Kymographs towards bleb-free regions within the same time-frames of the movie were selected as the controls. The results were plotted as histograms to display the variance in flow direction and velocities, by pooling together 10 tracks from each analyzed cell.

Analysis of *F*-actin network density at the contact center
Ftractin-mNeonGreen-labeled F-actin networks, excluding the contact rim, were extracted using SOAX, a software for quantification of biopolymers networks.[79] For time-lapse images, parameters were adjusted for each movie based on inspection of some frames and the corresponding extracted networks; the saved parameters were later on used to batch process the movies. Using a custom Python script, total network lengths were measured with Skan library functions and divided by contact areas to get network density values.[90] Radial network density profile was calculated with the 1-pixel-thick network map as described above.

Single particle tracking and analysis of Actin lifetime
TRITC-Actin-injected cells were imaged on the Imic TIRF microscope with ~100 nm pixel size, using a 561-nm laser line with 100 ms exposure. Acquisition intervals of 1 s, 2 s and 3 s were used to capture time lapses of at least 200 frames. Particle detection and tracking were performed using the TrackMate plugin in Fiji, based on a Gaussian fit with an estimated diameter of 0.3 μm. Linking distance of a maximum of 0.2 μm and gaps of a maximum of 2 frames were allowed to account for failures to detect particles. Thresholds were adjusted manually for each experiment and tracks were verified by overlaying with the raw data. Average lifetime of Actin at contacts was calculated using a previously described method.[91,92] Briefly, effective lifetime was obtained by fitting a monoexponential decay function to the lifetime distribution of trajectories obtained from each cell (Figure S5D). This value was corrected for photobleaching by using the varying acquisition intervals to obtain a photobleaching constant, on the basis of which a corrected dissociation rate could be calculated (Figures S5E and S5F).

Quantification of bleb frequency
Standard deviation projections of time-lapse movies of the contact were made using Fiji to define a stable contact zone. Blebs that extended and retracted back to this stable zone were manually counted for different conditions.

UV laser ablations
Cuts were performed on the F-actin network at the contact, for adhering cells on bilayers decorated with EcadECD both at the contact center or at the rim parallel to the contact edge, and for non-adhering cells on bilayers lacking EcadECD only at the center, by cutting along an 8 μm line with 12 UV pulses at 5 kHz. Subsequent imaging was performed to record the linear recoil for 5 s with 90 ms

intervals. A line perpendicular to the cut was used to generate a kymograph from which the opening distance after ablation was segmented, and a linear fit was performed on distance versus time measurements to extract recoil velocities. Cases where a wound response after UV ablation was detected were excluded from the quantification.

Theoretical modeling of flow-mediated rim accumulation

For any specie with concentration profile $c(x, t)$ at position x along the contact (in the center-rim axis) and time t, conservation law dictates that $\partial_t c = -\partial_x cv + R(c)$ where $v(x, t)$ is the local velocity and $R(c)$ local turnover/reaction rates. This simply indicates that local density changes can occur only from velocity gradients or local reactions. The simplest expression for $R(c)$ is first-order kinetics $R(c) = \frac{c_0 - c}{\tau}$, which simply assumes that the specie c turns over with a well-defined time scale τ to a target density c_0 (note that both τ and c_0 could in principle depend on time and/or other species, which we neglect here to check whether the simplest model of flow and constant turnover fits the data). The assumption of first-order kinetics was further tested by the fact that it predicts a simple exponential recovery upon FRAP, which fitted well with the data (Figures 3D' and 3E). The first of our modeling approaches is to take the velocity field as a given and calculate the resulting profile of specie $c(x, t)$. Based on the data, the simplest expression for velocity is $v(x, t) = \frac{\pi v_0}{2} sin(2\pi x / L)$, which is zero both at $x = 0$ (middle) and $x = L/2$ (rim), and has average velocity of v_0 (the experimentally measured parameter, alongside the contact diameter L). This leads – to first order – to a sinusoidal density profile $c(x, t) = \frac{\pi^2}{L} \frac{v_0}{\tau} cos(2\pi x/L)$, from which we can predict the normalized rim accumulation as $\boldsymbol{A} = \frac{\boldsymbol{c(0, t)}}{\boldsymbol{c(L/2, t)}}$ as discussed in the main text. Note that we can also easily incorporate in this model the possibility of immobile fractions, for instance, in Ecad. This can be done by writing two different equations for mobile and immobile Ecad (resp. c_m and c_i) $\partial_t c_i = -\partial_x c_i v + R(c_i)$. For truly immobile Ecad, we would have $R(c_i) = 0$, however, this is pathological for long-time scales as all Ecad would rapidly concentrate at the very rim. As we are looking at contacts on the 1-10 min time scale, we simply assume a second fraction with much slower turnover than the mobile fraction $R(c_i) = \frac{c_{i0} - c_i}{\tau_i}$, with $\tau_i = 3\,min$. This only causes mild increases in rim accumulations of Ecad. Although we have mainly focused on the steady-state rim-to-center accumulation and density profiles, it should be noted that the model can also predict the dynamics of rim accumulation (Figure S5A), which can be directly compared to the experimental time course (Figure S5B). In principle, one could also model explicitly actomyosin flows on an expanding spatial domain (to consider their interplay with contact growth). However, our data are consistent with a two-phase model - where the bulk of contact growth occurs in the first minutes of contact formation (driven biochemically by Myosin-2 down-regulation at the contact, Figures 1B and 1C), while flow-driven rim accumulation occurs mainly in a second phase of contact maturation (Figures S3B, S3F, and S3F'). This means that the two processes can be largely modeled independently from each other: when investigating the growth of contact area $A(t)$, we can write it as force balance between Myosin-2 contractility at the contact $f_c(t)$ and at the poles f_p (taken constant in time), which would predict a negative correlation between average Myosin-2 at the contact and contact area, with a small delay related to cell-substrate friction. Indeed, when calculating the cross-correlation between the two, we find a robust negative correlation across samples (Figure S2E), with little time lag, arguing that contact area growth in the first phase is directly related to Myosin-2 downregulation at the contact.

The second step of the modeling is then to ask how the velocity field $v(x, t)$ is determined in the first place. For this, we use the classical isotropic active gel theory, which has been shown to be a minimal description of actomyosin mechanics, and has as input parameters the contractility of actomyosin χ, the viscosity of the gel η and the friction to the substrate ξ. The force-balance equation combined with constitutive active gel equation then reads: $-\xi v = \eta \partial_{xx} v - \chi \partial_x \rho$ where ρ is the local actomyosin concentration, also following the conservation equation described above, which has to be complemented with a small diffusion coefficient for stability $\partial_t \rho = -\partial_x \rho v + D\partial_{xx} \rho - \frac{\rho - \rho_0}{\tau_\rho}$. This minimal model has been shown to give rise to spontaneous instabilities, where local accumulations of actomyosin create flows that sustain them despite turnover. Theoretically, this occurs when contractility is above a threshold $\chi_c = (\sqrt{D\xi} + \sqrt{\eta/\tau})^2$. Below the contractility threshold, although spontaneous accumulations are not formed, introducing spatial heterogeneities in the model can lead to strongly self-reinforcing flows. For instance, if we assume that the rim is characterized by slightly larger actomyosin contractility $\chi(1 + \delta\chi)$ than the center of the contact, this will create flows towards the rim, creating density gradients in ρ which will self-reinforce flows. Interestingly, applied to our data, this suggests that the contacts of control cells might not be above this threshold (as the patterning is not spontaneous, but instead always strongly guided from the start towards the contact rim) (Figures S3B, S3F, and S3F'), while the contacts of LPA-treated cells, characterized by strongly increased contractility, show the hallmarks of such local and self-organized accumulations (Figures 2E and 2E'). Based on our findings that RhoA remains more active at the rim of the contact compared to the center (Figure 2A), even in the first minutes of contact formation (i.e. prior to flow establishment) (Figure S3B), we input in our simulation a higher contractility at the rim, which we take δ=33% under the simple assumption that contractility is proportional to local RhoA activity. As we discussed in Figure 5, we have also evidence that this local increase of contractility at the ring is driven by blebs, although the model is agnostic as to the source of the increase. Note that in this model, the observed flux of F-actin filaments comprises both diffusion and advection, so we plot in the model the total velocity $v_{tot} = v - D\frac{\partial_x \rho}{\rho}$. We take the turnover time τ_ρ and contact diameter as previously measured. The viscosity η can be used to rescale force balance so we set it to 1 without loss of generality, while the ratio of friction to viscosity ξ/η is taken as $\xi/\eta = 1/100\,\mu m^{-2}$ based on measurements in other systems,[47] and in order to have flows propagate on the length scale of the entire contact as observed experimentally (Figure S3E). The diffusion coefficient - which does not play a key role apart from smoothing the velocity field - is taken to be small $D = 0.1\,\mu m^2/s$.[55] Taking a rescaled contractility $\chi/\eta = 2.25$ could reproduce well the average velocity observed in contacts of normal (wild type) cells, as well as the observed velocity and density profile of F-actin as a function of position (Figure S5C; see also Figures 2A and S3F). Modeling contacts of LPA-treated cells as moderately larger values for contractility of $\chi/\eta = 2.75$ would result in increased rim-to-center accumulation, but also in a doubled velocity due to the self-reinforcing loop operating via actomyosin flows,

where initial biases in contractility create flows which reinforce the contractility differences between rim and center (Figure S5C). Interestingly, in experiments, flows in contacts of LPA-treated cells are comparable in amplitude to the ones measured in untreated cells despite the increased contractility, which can occur if either the friction or viscosity of the actomyosin gel is increased by LPA treatment (e.g. due to stronger link to the substrate or higher cross-linking from Myosin of the active gel, respectively - see Figure S5C for exploration of the effects of friction or viscosity). Although this value is still below the threshold for purely self-generated instabilities in the absence of any guiding cues, local and stochastic increases in contractility can still lead to local flows and actomyosin accumulation,[55] reminiscent of the local foci that we sometimes observe under LPA treatment (Figure 2E). Interestingly, localized accumulations have been recently predicted in similar models of active cytoskeleton additionally considering the dynamics of activators,[93] a possibility that needs to be further explored for cell contact formation.

QUANTIFICATION AND STATISTICAL ANALYSIS

Statistical tests were performed in Graphpad Prism 6. Details for each experiment are described in figure legends. In brief, a D'Agostino-Pearson normality test was first performed, and, based on the results, a two-tailed Student's t-test for parametric distributions and a Mann-Whitney U-test for non-parametric distributions were used to compare two groups. To compare more than two groups, an ANOVA test for parametric distributions and a Kruskal-Wallis test for non-parametric distributions were used. The experiments were repeated at least 3 independent times, where controls and experiments were performed within the same egg-lay. n denotes the number of cells analyzed.